ATP-Competitive Partial Antagonists of IRE1α's RNase Segregate Outputs of the UPR

Hannah C. Feldman[1], **Rajarshi Ghosh**[2,4,5,6,7], **Vincent C. Auyeung**[2,4,5,6,7], **James L. Mueller**[2,3], **Jae-Hong Kim**[2,4,5,6,7], **Zachary E. Potter**[1], **Venkata N. Vidadala**[1], **B. Gayani K. Perera**[1], **Alina Olivier**[2,4,5,6,7], **Bradley J. Backes**[2,4], **Julie Zikherman**[2,3], **Feroz R. Papa**[2,4,5,6,7], **Dustin J. Maly**[1,8]

[1]Department of Chemistry, University of Washington, Seattle, Washington, USA

[2]Department of Medicine, University of California– San Francisco, San Francisco, California, USA

[3]Division of Rheumatology, Rosalind Russell and Ephraim P. Engleman Arthritis Research Center, University of California– San Francisco, San Francisco, California, USA

[4]Lung Biology Center, University of California– San Francisco, San Francisco, California, USA

[5]Department of Pathology, University of California– San Francisco, San Francisco, California, USA

[6]Diabetes Center, University of California– San Francisco, San Francisco, California, USA

[7]Quantitative Biosciences Institute (QBI), University of California– San Francisco, San Francisco, California, USA

[8]Department of Biochemistry, University of Washington, Seattle, Washington, USA

Abstract

The unfolded protein response (UPR) homeostatically matches endoplasmic reticulum (ER) protein-folding capacity to cellular secretory needs. But under high/chronic ER stress, the UPR triggers apoptosis. This dichotomy is promoted by differential activation of the ER transmembrane kinase/endoribonuclease (RNase) IRE1α. We previously found that IRE1α's RNase can be either fully activated or inactivated by ATP-competitive kinase inhibitors. Here we developed kinase inhibitors—'PAIR's—Partial Antagonists of IRE1α RNase—that partially antagonize IRE1α's RNase at full occupancy. Biochemical and structural studies show that PAIRs promote partial RNase antagonism by intermediately displacing the αC helix in IRE1α's kinase domain. In insulin-producing β-cells, PAIRs permit adaptive XBP1 mRNA splicing, while quelling

destructive ER mRNA endonucleolytic decay and apoptosis. By preserving XBP1 mRNA splicing, PAIRs allow B-lymphocytes to differentiate into immunoglobulin-producing plasma cells. Thus, an intermediate RNase-inhibitory "sweet spot", achieved by PAIR-bound IRE1α captures a desirable conformation for drugging this master UPR sensor/effector.

Introduction

Overwhelming the protein folding and structural maturation capacity of the early secretory pathway leads to accumulation of misfolded and immature secretory proteins in the endoplasmic reticulum (ER).[1] Eukaryotic cells evolved intracellular signaling pathways to respond to such "ER stress". These "Unfolded Protein Response" (UPR) pathways maintain cellular secretory function and physiological health in the face of remediable ER stress.[2] First discovered in unicellular eukaryotes, UPR pathways promote homeostatic/adaptive outputs through transcriptional upregulation of ER protein-folding and quality-control factors that extract terminally misfolded proteins back to the cytosol for degradation.[3,4] However, in mammalian cells experiencing irremediable ER stress levels that cannot be mitigated by these adaptive arms, the UPR triggers programmed cell death (PCD), typically through mitochondrial apoptosis.[2] Multicellular organisms likely benefit from culling irreversibly ER-stressed cells because of the potential harm caused by secreting misfolded protein cargo. However, in chronic states of such "terminal" UPR activation, the cumulative decrement of cell numbers through unchecked PCD may actively promote cell degenerative diseases.[5]

One critical life-death switch in the UPR is governed by the ER transmembrane multi-domain sensor protein, IRE1α.[6] IRE1α is activated upon ER stress elevation, causing this sensor to self-associate in the ER membrane. This event causes IRE1α's cytosolic kinase domain to trans autophosphorylate, which results in subsequent activation of its C-terminal endoribonuclease (RNase) catalytic domain.[7–9] The range of available IRE1α RNase activation states runs a gamut from the inactive, the active, to the hyperactive, with the level of activity controlled by the proximal kinase module. Low-level activation of IRE1α's kinase/RNase promotes cleavage of the adaptive XBP1 transcription factor mRNA to initiate its frame-shift splicing, while high-level kinase/RNase hyperactivation expands the RNase substrate repertoire to myriad ER-localized mRNAs that become endonucleolytically cleaved in a process termed Regulated IRE1α Dependent Degradation (RIDD), thus initiating apoptosis.[6, 10–12]

For maintaining cellular homeostasis, *a priori*, the "sweet spot" for IRE1α RNase activation may lie at a level wherein adaptive XBP1 mRNA splicing remains permissible, but without the initiation of RIDD. The cellular effects of such a meta-stable activation state have been demonstrated with IRE1α mutants (some found naturally as somatic mutations in cancers that act as RNase hypomorphs) and chemical-genetic systems.[6, 10] While adenosine-5'-triphosphate (ATP)-competitive inhibitors can control endogenous IRE1α's RNase activity through the kinase domain, such allosteric modulators have largely been shown to enforce opposite *extremes* of activation states.[13–16] Therefore, an optimal mode of engaging endogenous IRE1α's ATP-binding site has hitherto been unachieved.

Here, we demonstrate that it is possible to design ATP-competitive inhibitors, which we named 'PAIR's—Partial Antagonists of IRE1α RNase—that fully engage IRE1α's kinase domain but only partially inhibit its RNase activity. By performing systematic structure-activity analyses of ATP-competitive inhibitors, we identified the chemical features that distinguish PAIRs from previously reported allosteric activators and full inhibitors of IRE1α. Through comparisons of inhibitor-bound IRE1α complexes, we find that the partial antagonism of PAIRs is a result of their ability to only intermediately displace helix-αC outward in IRE1α's kinase domain from an active conformation. We further show that enforcing such an optimal IRE1α inhibitory state in cells allows partial antagonism of the RNase, sufficient to permit adaptive XBP1 mRNA splicing, while mostly inhibiting RIDD. Finally, we show that PAIRs have the unique ability to segregate distinct biological outputs of IRE1α in cellular systems by chiseling away destructive (RIDD-dependent) cell fate outcomes from adaptive (XBP1 splicing-dependent) ones. Thus, PAIRs may represent a new pharmacological modality for addressing ER stress-induced cell degeneration by preserving an adaptive UPR while blunting terminal UPR outputs.

Results

ATP-Competitive Ligands Tune IRE1α's Dimerization Affinity

To better understand how to achieve an optimal RNase inhibitory state, we established an *in vitro* framework for quantitatively characterizing how kinase domain ATP-binding site occupancy affects IRE1α's RNase activity. Formation of a "back-to-back" dimer–characterized by an extensive interface between the kinase and RNase domains of each IRE1α protomer–is required for IRE1α's RNase domain to be catalytically active (Fig. 1a).[17–18] Phosphorylation of IRE1α's kinase activation loop stimulate RNase activity by promoting dimer formation.[14, 19] Furthermore, ligands that occupy the ATP-binding site of the kinase domain can also stimulate IRE1α's RNase activity by promoting dimer formation.[18, 20] We measured the ability of a purified kinase/RNase domain construct of IRE1α—IRE1α*—to cleave a fluorogenic XBP1 RNA mini-substrate as a function of IRE1α* concentration, in order to quantitatively determine IRE1α's dimerization affinity (K_{dimer}) (Fig. 1b). Using this assay, we found that IRE1α*, which is basally autophosphorylated on its activation loop, demonstrated a K_{dimer} in the high nanomolar range (Fig. 1c). A quantitatively dephosphorylated IRE1α* construct (dpIRE1α*) (Supplementary Fig. 1) was also capable of forming RNase-active dimers but with a much lower dimerization affinity (K_{dimer} >4 μM), showing that activation loop phosphorylation dramatically strengthens back-to-back dimer formation.

ATP-competitive ligands that allosterically promote IRE1α's RNase activity also increase the dimerization affinity of the kinase/RNase domains of IRE1α. We found that the K_{dimer} of dpIRE1α* was ~80 times lower when its kinase domain was complexed to the ATP-competitive ligands AT9283 or AZD7762 (Fig. 1d, Supplementary Fig. 2). AT9283 and AZD7762 also led to a similar fold increase in the dimerization affinity of IRE1α*, demonstrating that ATP-competitive ligands further promote dimer formation of activation loop-phosphorylated IRE1α (Fig. 1e, Supplementary Fig. 3).

Next, we tested how a class of ATP-competitive ligands—called Kinase Inhibiting RNase Attenuators ("KIRA"s)—that inactivate IRE1α's RNase activity through the kinase domain affect dimerization affinity.[13] We found that IRE1α* was unable to form RNase active dimers at any concentration tested when bound to the high affinity ligand, KIRA8 (**1**),[21] or even to a lower affinity KIRA, compound **2** (Fig. 1e, Extended Data Fig. 1). Thus, it appears that KIRAs stabilize an ATP-binding site conformation that almost completely disrupts the ability of IRE1α to form an RNase-active back-to-back dimer. This result is consistent with our observation that full-length IRE1α-mediated splicing of XBP1 mRNA was almost completely suppressed in ER-stressed insulinoma (INS-1) cells treated with KIRA8 (Extended Data Fig. 2), despite the accumulation of unfolded proteins that promote lumenal domain oligomerization. Thus, KIRA-bound IRE1α appears to be locked in an RNase-inactive monomeric state *in vitro* and in cells.

Partial Antagonists of IRE1α's RNase Activity

We speculated that it should be possible to identify ATP-competitive ligands that only intermediately weaken the dimerization affinity of IRE1α, and hence preserve some RNase outputs, unlike KIRAs that enforce a completely crippled RNase activity state. To better understand how to design such partial antagonists of IRE1α's RNase activity, we explored ATP-competitive ligands based on the pyridine-pyrimidine scaffold of KIRA8 (Fig. 2a, 2b). The pyridine-pyrimidine scaffold of KIRA8 makes extensive contacts with the ATP-binding site of IRE1α that are distal to regions that undergo major conformational changes upon dimerization, allowing the introduction of substituents that have the potential to differentially modulate dimer affinity while maintaining reasonable potency. We first generated and tested compound **3**, which contains a *trans*-hexanediamine and a 4-amino-3-fluorophenol at the R_1 and R_2 positions, respectively, of the pyridine-pyrimidine scaffold. We found that **3** dose-dependently inhibited the kinase activity of IRE1α and activated its RNase activity (Fig. 2c, Supplementary Fig. 4a, 5). In contrast, we observed that compound **4** (Fig. 2b, Supplementary Fig. 4b), which contains a 3-trifluoropropylsulfonamide group at the R_3 position but is otherwise identical to **3**, dose-dependently inhibited IRE1α*'s kinase and RNase activities (Fig. 2c) and completely suppressed the formation of RNase active dimers (Fig. 2d).

We reasoned that ATP-competitive ligands that are capable of partially antagonizing the RNase activity of IRE1α would likely contain R_3 substituents that are smaller than the 3-trifluoropropylsulfonamide group of **4**, but larger than those of **3**. Indeed, we found that compound **5**, which contains a 2-trifluoroethylsulfonamide R_3 substituent (Fig. 2b), quantitatively inhibited IRE1α*'s kinase activity but only partially (~80%) inhibited its RNase activity (Fig. 2e). Thus, only a small difference in the size of the substituent at the R_3 position can lead to partial versus complete inhibition of IRE1α*'s RNase activity. Based on this observation, we generated several additional ATP-competitive ligands (**6**, **7**, and **8** (hereafter, **8** will be referred to as PAIR1), Extended Data Fig. 3a–c) that provided quantitative kinase activity inhibition but only partially inhibited IRE1α's RNase activity (Extended Data Fig. 4); we named these compounds PAIRs, Partial Antagonists of IRE1α RNase. To demonstrate that partial inhibition was not contingent on scaffold, but rather the size of the R_3 substituent, we also generated compounds **9 (KIRA9)** and **10**, which

displayed quantitative inhibition of both IRE1α kinase and RNase domains (Fig. 2f, 2g, Extended Data Fig. 3d–f, 4b, c). As predicted, we found that this partial antagonism of RNase activity was a result of a weakened dimerization affinity rather than enforcement of a monomeric state (Fig. 2h, Supplementary Fig. 6). Thus, it was possible to design inhibitors that fully occupy IRE1α's ATP-binding site, yet only partially antagonize its RNase activity.

PAIRs Stabilize a Partially-Displaced Helix-αC

To provide mechanistic insight into the partial RNase antagonism of PAIRs, we obtained a 1.85 Å resolution co-crystal structure of PAIR1 bound to IRE1α*. As expected, PAIR1 occupies the ATP-binding site of IRE1α*, with the pyrimidine-pyridine scaffold forming two hydrogen-bonding interactions with the hinge region. Additional interactions include a hydrogen-bonding interaction between the naphthyl sulfonamide group and the backbone of the DFG-motif and a salt bridge between the piperidine substituent of PAIR1 and Glu651 in the α-H helix (Fig. 3a, Supplementary Table 1). These aforementioned interactions are highly similar to those made between IRE1α* and the KIRAs AMG-16 (**11**) (PDB: 4U6R) and KIRA8 (PDB: 6URC), which share the same pyrimidine-pyridine scaffold as PAIR1 (Supplementary Fig. 7).

We speculated that differences in how PAIRs and KIRAs influence the conformation of the helix-αC could explain the variable effects that they have on dimerization affinity. Helix-αC is a dynamic regulatory element that lines IRE1α*'s ATP-binding pocket; when it is in the active conformation it forms a significant portion of the RNase active back-to-back dimer interface.[14] Consistent with the ability of PAIR1 to partially inhibit IRE1α*'s RNase activity, helix-αC of the PAIR1-IRE1α* complex is rotated and displaced from the active conformation (Supplementary Fig. 8). Superimposition of the PAIR1-IRE1α* structure with IRE1α* bound to the KIRA AMG-16, which also presents its R_3 sulfonamide from the 4-position of a 4-amino-1-naphthol ether R_2 group, shows that the more compact 2-trifluoroethanesulfonamide R_3 substituent of PAIR1 leads to a smaller displacement of the helix-αC from the active conformation compared to a 2-chlorophenylsulfonamide (Fig. 3b, Extended Data Fig. 5). PAIR1 also leads to a smaller displacement of helix-αC than KIRA8 (Extended Data Fig. 5c). Thus, the fact that PAIRs partially displace helix-αC from an active conformation likely explains why they only reduce IRE1α*'s dimerization affinity.

The differences that we observe between PAIRs and KIRAs in their modulation of IRE1α*'s dimerization affinity in solution appear to be reflected in the oligomeric states of the PAIR1-IRE1α* and AMG-16-IRE1α* complexes in crystal structures.[21] We observed that PAIR1-bound IRE1α* crystallized as a back-to-back dimer, while the AMG-16-bound structure of IRE1α* was monomeric (Fig. 3c). However, the structure of the PAIR1-IRE1α* dimer is not identical to the RNase-active dimer. While a majority of the interface contacts that the RNase active dimer forms are conserved in the PAIR1-IRE1α* structure, an inter-dimer salt bridge between Asp620 and Arg594/Arg627, which was identified in a previous study as an essential interaction in IRE1α's formation of RNase active dimers, is partially disrupted (Extended Data Fig. 6).[22] Thus, PAIR binding leads to only a limited perturbation of IRE1α*'s dimer interface unlike KIRAs.

PAIR1 Preserves XBP1 Splicing but Blocks RIDD

Prior to conducting cellular studies with PAIRs, we performed kinome selectivity profiling using a chemical proteomic method (Fig. 4a).[23–25] Specifically, we measured the ability of **2**, **3**, **6**, **7**, PAIR1, and KIRA9 to compete with lysate kinases for binding to a nonselective kinase inhibitor matrix (kinobeads). Each compound (10 µM) was incubated with a standard kinobead matrix and a HEK293/HCT116 lysate mixture and competed kinases were quantified. We found that all four PAIRs displayed high selectivity for IRE1α, with only a few off-target kinases observed (Figure 4a, Supplementary Fig. 9, 10). We selected PAIR1 for further studies because of its high selectivity for IRE1α and the availability of a KIRA, KIRA9, that only differs by one methylene group with equivalent potency and selectivity.

We next tested PAIR1 and KIRA9 in an INS-1 stable cell line where IRE1α activation can be achieved through doxycycline (Dox)-inducible overexpression of a mouse IRE1α transgene.[6] We have previously demonstrated that this maneuver causes IRE1α to spontaneously self-associate and autophosphorylate, triggering RIDD, and subsequently causing entry into mitochondrial apoptosis, without the use of pleiotropic ER stress-inducing agents. Using phostag-acrylamide gels, we found that both PAIR1 and KIRA9 were able to equivalently block the autophosphorylation induced by conditional overexpression of IRE1α in these lines at almost identical concentrations (Fig. 4b). Thus, PAIR1 and KIRA9 were able to fully engage the ATP-binding site of full-length, cellular IRE1α at comparable levels.

In contrast to KIRA9, we observed that PAIR1 largely preserved XBP1 mRNA splicing and expression of the frame-shifted Xbp1s transcription factor protein in these cellular systems, despite equivalent kinase domain engagement at the concentration tested (Fig. 4c, Supplementary Fig. 11). Likewise, PAIR1 only weakly inhibited XBP1 mRNA splicing in INS-1 cells and human islets subjected to ER stress-inducing agents (Fig. 4d, 4e, Extended Data Fig. 7). However, consistent with the notion that downstream RIDD should be equivalently blunted by PAIRs and KIRAs, we found that the RIDD substrates Blos1 and the mRNAs encoding proinsulin (Ins1 and Ins2 in rodents) were rescued by both PAIR1 and KIRA9 (Fig. 4f–4h).[10] The recovery of Ins1/Ins2 mRNA led to increased levels of proinsulin protein (Fig. 4i). Likewise, both PAIR1 and KIRA9 were also able to equivalently blunt RIDD in ER-stressed INS-1 cells (Fig. 4j).

PAIRs and KIRAs Block ER-localized mRNA Decay and Apoptosis

Next, to systematically compare the transcriptomic effects of PAIR1 and KIRA9, we profiled INS-1 cells that conditionally overexpress IRE1α by RNA-Seq. As above (Fig. 4), cells were treated with either DMSO, or equivalent concentrations of PAIR1 or KIRA9 and IRE1α overexpression was induced with Dox. Total RNA was submitted for sequencing across entire transcripts. We observed that Dox treatment led to >10-fold induction of the mouse IRE1α transgene (Supplementary Fig. 12) and the dense coverage across the *Xbp1* locus enabled quantification of XBP1 splicing based on the reduced density of reads mapping to the noncanonical XBP1 intron. Consistent with measurements of XBP1 splicing by isoform-specific PCR (Fig. 4c), overexpression-induced XBP1 mRNA splicing was preserved in both DMSO and PAIR1-treated cells but blocked in KIRA9-treated cells at 4 hours (Supplementary Fig. 13). At 24 hours, when XBP1 mRNA splicing is saturated,

splicing levels were still partially decreased in KIRA9-treated cells, yet preserved in the presence of PAIR1 (Supplementary Fig. 13).

We next interrogated RIDD target gene expression in these cells (Fig. 5a). Previously, we showed that overexpression of IRE1α induced the endonucleolytic degradation of a population of mRNAs enriched for those predicted to be ER-localized, such as those encoding ER-resident or ER-cargo proteins (i.e."secretome"), as occurs naturally during ER stress regimes.[6] We were able to recapitulate the "RIDD signature" we defined previously in this model. Furthermore, downregulation of RIDD signature genes was antagonized by both PAIR1 and KIRA9 to a similar degree (Fig. 5a). Indeed, "secretome" transcripts were globally decreased by IRE1α overexpression when compared to controls.[26] This effect was blocked by both PAIR1 and KIRA9 (Supplementary Fig. 14), consistent with a model whereby IRE1α docks to the translocon and upon hyperactivation and oligomerization degrades nearby mRNAs being translated on ER membrane-associated ribosomes during the process of co-translational translocation of the nascent, emerging polypeptides (encoded by these ER-localized mRNAs) while they are being synthesized.[27]

A priori, if XBP1 mRNA splicing inhibition is irrelevant for entry of cells into apoptosis—while RIDD promotes apoptosis—then both PAIR1 and KIRA9 should perform equivalently to each other in cytoprotection assays, because they share the common feature that they cause equivalent rescue of RIDD. Consistent with this notion, we observed that both PAIR1 and KIRA9 markedly reduced the generation of cleaved caspase-3 and showed significant and similar cytoprotective efficacy in a mitochondrial apoptosis assay (Annexin-V positivity) (Fig. 5b, c). We previously showed that IRE1α's RIDD activity promotes apoptosis by upregulating a pro-oxidant mediator and amplifier of terminal UPR signaling, thioredoxin-interacting protein (TXNIP), in INS-1 cells that overexpress IRE1α.[10, 28] We found that Txnip mRNA upregulation was blocked by both PAIR1 and KIRA9 (Fig. 5d, *top row*). More generally, to the extent that pro-apoptotic genes (Gene Ontology term GO004065: positive regulation of apoptotic process) were upregulated by IRE1α overexpression, these changes were largely blunted to similar degrees by either PAIR1 or KIRA9 (Fig. 5d). Together, these results affirm that even though PAIRs only partially antagonize IRE1α's RNase (leaving XBP1 mRNA splicing extant), their ability to inhibit RIDD like KIRAs is fully sufficient to block the destructive effects of the terminal UPR leading to apoptosis.

PAIRs Permit B-Lymphocyte Differentiation into Plasma Cells

We next asked: where should the effects of separating XBP1 mRNA splicing away from RIDD have discriminatory biological effects? We decided to interrogate the adaptive immune response to infection, through which naïve B-lymphocytes must undergo a complex maturation process, including radical expansion of the ER and associated protein folding machinery, ultimately becoming plasma cells that are capable of secreting massive quantities of antibodies. As a master regulator of the UPR, IRE1α's initiation of XBP1 splicing is required for maturation of B-lymphocytes into plasma cells, in an adaptive UPR.[29–31] Since KIRAs and PAIRs have divergent effects on XBP1 splicing, we reasoned that they would have corresponding differential effects on plasma cell maturation. Prior to performing

these experiments, we identified a more potent PAIR, PAIR2 (**12**), that could be used as a comparator to KIRA8 (Extended Data Fig. 8). PAIR2 demonstrated a similar ability to inhibit IRE1α's kinase activity as KIRA8 *in vitro* and in cells (Extended Data Fig. 8b, c). Pre-treating INS-1 cells with PAIR2 prior to provision of KIRA8 (added at a concentration that leads to significant inhibition of XBP1 splicing (Extended Data Figure 8d)) prevents KIRA8's inhibition of ER stress-induced XBP1 splicing (Extended Data Figure 8e). Thus, PAIR2 is capable of completely occupying IRE1α's ATP-binding site in cells and can block the ability of a potent KIRA to inhibit XBP1 splicing. Furthermore, PAIR2 exhibited high selectivity in our kinome selectivity profiling assay (Extended Data Figure 8f, g).

With two matched sets of PAIRs and KIRAs in hand, we next assessed how KIRA8, KIRA9, PAIR1, and PAIR2 affect the differentiation of lipopolysaccharide (LPS)-treated mouse splenocytes into antibody-secreting plasmablasts.[32] As expected, flow cytometric analysis showed that LPS treatment of B-cells led to enhanced proliferation and expression of intracellular XBP1s (Fig. 6a, b), a modest increase in live B-cell numbers, and dramatically increased plasma cell differentiation as assessed by upregulation of CD138 expression and B220 downregulation relative to untreated splenocytes (Fig. 6c, d, Extended Data Fig. 9, 10). LPS treatment also correspondingly increased plasma cell secretion of IgM into the culture media (Fig. 6e, 6f). Splenocytes incubated with either KIRA8 or KIRA9 prior to LPS treatment showed reductions in XBP1s expression, plasma cell differentiation, and IgM secretion in a dose-dependent manner that is in agreement with their relative *in vitro* potencies (Fig. 6a–d). By contrast, PAIR1 and PAIR2 were highly permissive for XBP1s expression, plasma cell differentiation and IgM secretion at all concentrations tested (Fig. 6e, 6f).

Finally, we confirmed that LPS treatment of splenocytes triggered elevations in XBP1 mRNA splicing, which were reversed with KIRA9, but not with PAIR1 (Supplementary Fig. 15a), as in the INS-1 and islet experiments shown previously. Like INS-1 cells and human islets treated with ER stress and in INS-1 overexpressing IRE1α, LPS treatment caused decay of Blos1 mRNA, which was rescued with either PAIR1 or KIRA9 (Supplementary Fig. 15b).

Discussion

In the unicellular eukaryote, *S. cerevisiae*, Ire1 initiates non-conventional splicing of the mRNA encoding the Hac1 transcription factor-encoding mRNA[33, 34]; in another unicellular eukaryote, *S. pombe*, Ire1 exclusively promotes RIDD.[35] In both these model organisms, Ire1's enzymatic outputs physiologically restore ER secretory homeostasis during ER stress. In contrast to these unicellular eukaryotes, multicellular eukaryotes—especially mammals—have evolved an expanded number of UPR physiological outputs, and other UPR sensor/effectors. Yet the IRE1α ortholog in mammalian cells has preserved *both* non-conventional mRNA splicing of the mRNA encoding the XBP1 transcription factor *and* RIDD.[6, 12] We first bifurcated these two outputs in mammalian cells through chemical-genetics that enforce XBP1 mRNA splicing while averting RIDD, through provision of the orthogonal kinase inhibitor 1NM-PP1 to drug-sensitized IRE1α mutants.[6, 10, 11] We also previously

developed ATP-competitive ligands, which we named KIRAs, that fully antagonize IRE1α's two RNase outputs at maximal occupancy.

Here, we developed ATP-competitive ligands–PAIRs–that partially antagonize endogenous IRE1α's RNase activity at maximal occupancy of the kinase, which allows inhibition of RIDD, while still preserving XBP1 mRNA splicing. Our biochemical and structural studies inform a cellular model wherein at maximal kinase occupancy the partial antagonism afforded by PAIRs allows the preservation of dimeric IRE1α species that are sufficient for adaptive XBP1 mRNA splicing, while the higher-order oligomeric species needed for RIDD are prevented from forming (Supplementary Fig. 16a). In contrast, KIRA-bound IRE1α is monomerized at full kinase occupancy(Supplementary Fig. 16b); thus, at maximal occupancy, PAIRs mimic the ability to splay apart the inhibition of XBP1 mRNA splicing from the inhibition of RIDD, which KIRAs can only achieve at sub-maximal occupancy (Supplementary Fig. 16c).

We were able to achieve this partial antagonism by introducing substituents into PAIRs that only intermediately displace the helix-αC of IRE1α's kinase domain from an active conformation. The helix-αCs of protein kinases are dynamic structural features that are often allosterically coupled to distal binding interfaces.[37, 38] In many cases, helix-αC's conformation has been defined as two conformational extremes; an active "in" form or an inactive "out" conformation. PAIRs stabilize an intermediate conformational state between these two extremes, which appears to mimic unphosphorylated *apo* IRE1α based on the similar K_{dimer}s of PAIR-bound IRE1α and unphosphorylated *apo* IRE1α. As the helix-αCs of many kinases are components of binding interfaces, it is likely that similar partial allosteric antagonism can be engineered into ATP-competitive inhibitors that target other kinases.

The "Janus-like" nature of IRE1α's cytosolic RNase outputs is a challenge for the development of therapeutic modulators for treating diseases of ER stress-induced premature cell death. One RNase output, the cleavage of XBP1 mRNA, is critical to several adaptive responses to stress and cellular ontogenic processes.[8, 39, 40] The other RNase output, IRE1α-mediated RIDD, contributes to degenerative disease by promoting apoptosis in cells, including the β-islet cells of the pancreas.[6, 12, 41] Prior to this work, small molecule inhibitors of IRE1α's RNase blocked both of these outputs in tandem. PAIRs, therefore, represent a new modality for allosterically controlling IRE1α's RNase activity–stabilizing an intermediate conformational state that splits apart and segregates downstream RNase outputs.

Our newfound ability to bifurcate the RNase outputs of IRE1α with PAIRs creates the potential to drug the UPR in more nuanced ways than with existing modulators. We illustrated this by comparing the effect of a PAIR with a closely-matched comparator KIRA in two distinct IRE1α-mediated cell fate regimes—one "destructive" and the other "constructive". We predicted that if RIDD is necessary for apoptosis, then a KIRA and a PAIR would equivalently block RIDD and apoptosis. Indeed, this is what we found. The transcriptome of downregulated ER-localized mRNAs was largely superimposable between PAIR1 and KIRA9 treatment in INS-1 cells, as apoptotic gene upregulation

was equivalently quelled by both inhibitors in this RIDD-driven physiological system. By comparison, in the "constructive" model of *de novo* differentiation of B-cells into immunoglobulin-producing plasma cells, we observed differential effects between PAIRs and KIRAs. By inhibiting XBP1 mRNA splicing (an event that is required for building and expanding the ER physically and functionally during terminal differentiation), KIRAs demonstrated dose-dependent inhibitory effects on the production of CD138+ plasma cells. However, PAIRs were largely permissive for plasma cell differentiation, even at maximal kinase occupancy, while retaining XBP1 mRNA splicing. As in our β-cell models, reduction of Blos1 mRNA (a RIDD target) was rescued by both PAIRs and KIRAs.

Thus, we propose that the ability to segregate IRE1α's synthetic UPR outputs (i.e, XBP1 transcription factor-driven) from its destructive RIDD outputs through applying PAIRs as comparators to monomerizing KIRAs has the broad potential to reveal the scope and diversity of distinct UPR biological outputs. Finally, we predict that PAIRs may be superior to existing IRE1α kinase (KIRAs) and other (direct) RNase inhibitors for treating diseases in which preservation of XBP1 splicing is important for optimal efficacy and safety.[42–44] In sum, the unique ability of PAIRs to preserve adaptive XBP1 splicing at full target engagement promises to provide new tools for studying the UPR and may represent a more desirable therapeutic modulation of IRE1α in myriad diseases caused by ER stress-induced premature cell death.

Online Methods

Expression and purification of IRE1α* and dP-IRE1α*

A construct containing the cytosolic kinase and RNase domains of human IRE1α (residues 547–977, IRE1α*) was expressed in SF9 insect cells (ATCC, #CRL-1711) by using the Bac-to-Bac baculovirus expression system (Invitrogen) with a His6 tag at the N-terminus and purified with a nickel–nitriloacetic acid (Qiagen) column. To generate dP-IRE1α*, we removed basal phosphorylation sites by incubating IRE1α* with λ-PPase (New England Biolabs) at a molar ratio of 5:1 (IRE1α*: λ-PPase) in 50 mM HEPES pH 7.5, 100 mM NaCl, 1 mM $MnCl_2$, 2 mM dithiothreitol (DTT) and 0.01% Brij 35 detergent (v/v) overnight at 4°C. Dephosphorylation was verified through western blotting using a universal phospho-protein detection agent (biotin-pIMAGO (Tymora Analytical Operations, Cat. No.: FL800) and imaged using a streptavidin-linked fluorophore.

Western blotting and antibodies

For protein analysis, cells were lysed into modified RIPA buffer (50 mM Tris, 150 mM NaCl, 10 mM NaF, 1% NP40 (v/v), 0.25% sodium deoxycholate (w/v), 5% glycerol (v/v), pH 7.8) containing protease inhibitor (Pierce Protease Inhibitor Tablets and 1 mM PMSF) and phosphatase inhibitor (Phosphatase inhibitor cocktail 2 and 3, Sigma Aldrich) prior to gel loading. Western blots were performed using Any kD™ Mini-PROTEAN® TGX™ Precast protein gels (BioRad). Gels were ran using Tris-Glycine running buffer (25 mM Tris pH 8.6, 192 mM glycine, 0.1% SDS (w/v)) at 180 V. Gels were transferred to nitrocellulose paper using the TransBlot Turbo System (BioRad) at 25 V, 2.5 A for 15 minutes. Nitrocellulose blots were blocked for 30 minutes at room temperature with

Odyssey blocking buffer (Li-Cor). Primary antibodies were diluted into blocking buffer and incubated over night at 4 °C. Blots were washed 2x with TBST (20 mM Tris pH 7.5, 150 mM NaCl, 0.1% Tween-20) and incubated with near-infrared-dye-conjugated secondary antibodies (Li-Cor) for 1 hour at room temperature (dilution 1:10,000). Blots were imaged using a Li-Cor Odyssey IR Imager and quantitated using ImageStudio. The following primary antibodies were used in this study: rabbit anti-IRE1α mAb #14C10 (Cell Signaling, no. 3294, dilution 1:1,000), mouse anti-FLAG (DYKDDDDK) mAb (Sigma Aldrich, no. F3165, dilution 1:1,000), rabbit anti-spliced XBP1 (Cell Signaling, no. 12782, dilution 1:1,000), rabbit anti-caspase 3 (Cell Signaling, no. 9662, dilution 1:1,000), rabbit anti-cleaved caspase 3 (Cell Signaling, no. 9661, dilution 1:1,000), mouse anti-proinsulin (Santa Cruz Biotechnology, no. sc-9168, dilution 1:1,000), and rabbit anti-GAPDH (Santa Cruz Biotechnology, no. sc-25778, dilution 1:1,000).

In vitro kinase inhibition assays

Inhibitors (initial concentration of 10 or 60 μM, three-fold serial dilutions) were incubated with IRE1α* in cleavage buffer (20 mM HEPES, 0.05% Triton X-100 (v/v), 50 mM KCl, 1 mM MgCl$_2$, 1 mM DTT, pH 7.5) for 30 min, followed by incubation with 10 μCi [γ^{32}P] ATP(3,000 Ci mmol^{-1}, PerkinElmer) at 23 °C for 3 hours. Samples were then spotted onto glass fiber paper (Easytab-C Glass Fiber Filter Paper, Perkin Elmer) and washed twice with 0.5% phosphoric acid and autoradiographed using a GE Typhoon FLA 9000 Imager. Blots were quantitated using ImageQuant software. The percent inhibition was quantified by setting the background (no kinase well) as 0 and standardizing to IRE1α* without compound treatment (IRE1α* + DMSO). Dose-response curves were fit using "one-site fit logIC50" parameter using GraphPad Prism V.8 analysis software.

In vitro RNase inhibition assays

50 nM IRE1α* was incubated with inhibitor (initial concentration of 10 or 60 μM, three-fold serial dilutions) or DMSO for 30 min in assay buffer (20 mM Tris, 50 mM NaCl, 1 mM MgCl$_2$, 2 mM DTT, 0.05% Triton X-100 (v/v), pH 7.5). Assays were initiated by adding 10 μL of XBP1 mini-substrate (5'-Alex647-CAUGUCCGCAGCGCAUG-IowaBlack-FQ-3'; IDT) to the wells at a final concentration of 200 nM and a final well volume of 30 μL. Fluorescence was detected on a Perkin Elmer Envision Microplate Reader at excitation and emission wavelengths of 650 nm and 665 nm. Dose-response curves were fit using "one-site fit logIC50" parameter using GraphPad Prism V.8 analysis software. Residual RNase activity (Fig. 2f, Extended Data Fig. 4) was determined by subtracting maximally achieved percent RNase inhibition (indicated by plateau of dose-response curve) from maximally achieved percent kinase inhibition (indicated by plateau of dose-response curve).

In vitro determination of IRE1α*–inhibitor complex K$_{dimer}$s

IRE1α* or dPIRE1α* was titrated from either 2 μM or 4 μM in two-fold serial dilutions in assay buffer (20 mM Tris, 50 mM NaCl, 1 mM MgCl$_2$, 2 mM DTT, 0.05% Triton X-100 (v/v), pH 7.5) and incubated with 50 μM inhibitor for 30 minutes at room temperature. Assays were initiated by adding 10 μL of XBP1 mini-substrate (5'-Alex647-CAUGUCCGCAGCGCAUG-IowaBlack-FQ-3'; IDT) to the wells at a final concentration of 6 μM and a final well volume of 30 μL. Fluorescence was detected on a Perkin Elmer

Envision Microplate Reader at excitation and emission wavelengths of 650 nm and 665 nm. Reaction process was monitored real time in 10-second intervals for at least 30 minutes. Initial rates of XBP1-cleavage were determined for each respective IRE1α* of dpIRE1α* concentration. Specific activity was then determined by dividing rate (RFU/s) by the respective IRE1α* of dpIRE1α* used (RFU/s*[IRE1α]). K_{dimer} values were determined by fitting these values using the non-linear regression 'one-site total' binding parameter in GraphPad Prism V.8 analysis software.

Crystallization of IRE1α* + PAIR1

Protein production and crystallization—Expression of IRE1α was performed by Proteros according to previously established protocols. A purification protocol was established, and homogeneous protein was produced in preparative amounts using affinity and gel filtration chromatography steps. This procedure yielded homogenous protein with a purity greater than 95% as judged from Coomassie stained SDS-PAGE. This purified protein was used in crystallization trials employing both a standard screen with approximately 1200 different conditions and as crystallization conditions identified using literature data. Conditions initially obtained have been optimized using standard strategies, systematically varying parameters critically influencing crystallization, such as temperature, protein concentration, drop ratio, and others. These conditions were also refined by systematically varying pH or precipitant concentrations.

Data collection and processing—A cryo-protocol was established using PROTEROS Standard Protocols. Crystals were flash-frozen and measured at a temperature of 100 K. The X-ray diffraction data were collected from complex crystals of IRE1α with the ligand PAIR1 at the SWISS LIGHT SOURCE (SLS, Villigen, Switzerland) using cryogenic conditions. The X-ray source was PXII/X10SA and the wavelength was 1.0000 Å. The crystals belong to space group C 2. Data were processed using the programs: XDS and XSCALE.

Structural modeling and refinement—The phase information necessary to determine and analyze the structure was obtained by molecular replacement. A previously solved structure of IRE1α was used as a search model. Subsequent model building and refinement was performed according to standard protocols with the software packages CCP4 and COOT. For the calculation of the free R-factor, a measure to cross-validate the correctness of the final model, about 2.6% of measured reflections were excluded from the refinement procedure (see Supplementary Table 1). TLS refinement (using REFMAC5, CCP4) was carried out, which resulted in lower R-factors and higher quality of the electron density map. Automatically generated local NCS restraints were applied (keyword "ncsr local" of newer REFMAC5 versions). The ligand parameterization and generation of the corresponding library files were carried out with CORINA. The water model was built with the "Find waters" algorithm of COOT by putting water molecules in peaks of the Fo-Fc map contoured at 3.0 followed by refinement with REFMAC5 and checking all waters with the validation tool of COOT. The criteria for the list of suspicious waters were: B-factor greater 80 Å^2, 2Fo-Fc map less than 1.2σ, distance to closest contact less than 2.3 Å or more than 3.5 Å. The suspicious water molecules and those in the ligand binding site (distance to

ligand less than 10 Å) were checked manually. The Ramachandran Plot of the final model shows 92.6% of all residues in the most favored region, 6.7% in the additionally allowed region, and 0.4 % in the generously allowed region. The residues Met872(A) and Met872(B) are found in the disallowed region of the Ramachandran plot. They were either confirmed by the electron density map or could not be modeled in another sensible conformation. Structural analysis was performed using Pymol Version 2.0.5.

Kinome profiling and selectivity

Kinobead enrichment protocol—HEK293 and HCT116 cells were plated on 15 cm plates until 90% confluent and lysed into 750 μL modified RIPA buffer (50 mM Tris, 150 mM NaCl, 10 mM NaF, 1% NP40, 0.25% sodium deoxycholate, 5% glycerol, pH 7.8) containing protease inhibitor (Pierce Protease Inhibitor Tablets and 1 mM PMSF) and phosphatase inhibitor (Phosphatase inhibitor cocktail 2 and 3, Sigma Aldrich). Protein content was determined via Bradford assay. HEK293 and HCT116 lysates were combined in a 1:1 ratio and exogenous IRE1α* was added to the lysate at a final concentration of 33.3 nM. Lysate (300 μg per sample) was incubated and rotated end over end with 10 μM inhibitor or DMSO (1% v/v) for 1 hour at 4 °C. For kinase enrichment, 10 μL of 50% kinobead slurry (in 20% ethanol) was prepared by washing twice with 500 μL Mod. RIPA buffer. DMSO or inhibitor treated lysates were then added to the washed kinobeads and rotated end over end for 3 hours at 4 °C. After enrichment, the supernatant was aspirated off and the beads were washed twice with 500 μL ice cold Mod. RIPA buffer and three times with 500 μL ice cold TBS (50 mM Tris, 150 mM NaCl, pH 7.8) to remove detergent. Beads were resuspended in 25 μL of denaturing buffer (6M guanidinium chloride, 50 mM Tris containing 5 mM TCEP and 10 mM CAM, pH 8.5). The bead slurries in denaturing buffer were then heated to 95 °C for 5 min. After, the bead slurries were diluted 2-fold with 100 mM TEAB (triethylammonium bicarbonate buffer, pH 8.5). Then 0.4 μg of LysC (Wako) were added to the beads and the pH adjusted to 8–9 with 1 N NaOH. The mixture was agitated on a Thermomixer (Eppendorf) at 37 °C for 2 hr at 1400 rmp. After, the samples were diluted 2-fold with 100 mM TEAB and 0.4 μg of sequencing grade trypsin (Pierce) was added and the samples agitated for another 12 hr at 37 °C at 800 rpm in the Thermomixer. After the overnight trypsinization, samples were diluted 2-fold with Buffer A (5% ACN, 0.1% TFA) containing 1% formic acid and the pH adjusted to 2–3 with formic acid if necessary. Homemade StageTips were prepared by running 50 μL of Buffer B (80% ACN, 0.1% TFA, H₂O) through them followed by 50 μL of Buffer A (5% ACN, 0.1% TFA, H₂O).[45] Beads were spun down and supernatant was added directly to StageTips. Following sample loading, StageTips were washed with 50 μL of Buffer A and eluted with 50 μL Buffer B. Samples were speed vacuumed until dry and re-suspend in Buffer A for injection onto LC-MS.[24]

LC-MS and data analysis—Tryptic peptides were separated using a nanoAcquity UPLC instrument with 10 cm fused silica capillary columns made in house and packed with 5 μm 120 Å reverse-phase C18 beads (ReproSil-Pur®, Maisch). Liquid chromatography was performed over 120 minutes using and initial 20 minute isocratic trapping of 3% Buffer B and a flow rate of 700 nL/min followed by a 100 minute gradient of 35% Buffer B to 80% Buffer B gradient at 350 nL/min. LC Buffer A solvent was 0.1% acetic acid in water and LC

Buffer B was 99.9% ACN, 0.1% acetic acid. MS data was analyzed using a Thermo Orbitrap Fusion Tribrid. Raw files were analyzed using MaxQuant (Andromeda) Version 1.6.0.16. Files were analyzed further using Perseus (Version 1.6.0.7) by filtering LFQ intensity values only identified by site, reverse, or potential contaminant. Missing LFQ intensity values were imputed in Perseus from a standard distribution downshifted by 1.8 and having a width of 0.4. To determine kinases that were significantly competed by treatment with 10 μM of inhibitor we applied a two-tailed two-sample t-test in Perseus with an FDR of 0.05. Kinases were reported as being non-competed by an inhibitor if it had a Log_2 LFQ ratio (Log_2 Difference) <1.0. Kinome tree visualization plots were created using CORAL and heat maps were made using GraphPad Prism V.8.[46] A detailed explanation of MS settings and search parameters, in addition to the complete proteomic dataset can be found in Supplementary Dataset 1.

Phostag acrylamide gels

Treatment conditions for phostag gels—INS-1 or IRE1α-overexpressing isogenic INS-1 cells were plated onto a 24-well Poly-D-Lysine coated tissue culture plate and grown for 48 hrs. Inhibitor or DMSO were added to the media and incubated for 1 hour at 37 °C with 5% CO_2 prior to addition of ER stress agents. After the 1 hour inhibitor incubation, cells were treated 200 μg/mL BFA (Sigma, Prod. No.: B6542) for 2 hours or 5 ng/mL doxycycline (Sigma) for 6 hours, with care to ensure the total DMSO concentration in the media did not exceed 1% (v/v). Cells were lysed directly into SDS loading buffer (50 mM Tris, 100 mM DTT, 2% SDS (w/v), 10% glycerol (v/v), and 0.1% bromophenol blue (w/v), pH 6.8) and boiled for five minutes prior to gel loading.

Phostag acrylamide gel procedure—IRE1α phostag acrylamide gel recipe has been previously established and was followed verbatim for this study.[47] Resolving gels were allowed to solidify (~1.5 hr) before adding the stacking gel and comb and allowed to solidify (~1 hr). Gels were run using Tris-Glycine-SDS running buffer (25 mM Tris, 192 mM glycine, 0.1% SDS, pH 8.3) at 100 V for 3–3.5 hours. After the gels were run, they were transferred onto nitrocellulose membranes via rapid transfer using a Transblot Turbo and premade transfer packs. Gels were transferred at 25 V, 2.5 A for 15 minutes. Nitrocellulose membranes were then subjected to standard western blotting procedures.

Tissue culture

INS-1s (rat insulinoma beta cells) were grown in RPMI, 10% FBS buffer (v/v), 1 mM sodium pyruvate, 10 mM HEPES, 2 mM glutamine and 50 μM β-mercaptoethanol on Poly-D-Lysine coated tissue culture flasks. IRE1α (murine) was cloned into a pcDNA5/FRT/TO. INS-1 FRT/TO cells were grown following the protocol above. INS-1 FRT/TO cells were transfected with 2 μg IRE1α-pcDNA5/FRT/TO and 2 μg pOG44 using Lipofectamine 2000 (Thermo Fisher). Cell media was exchanged the next day and cells were grown for another day before passaging. Selection was performed using 50 μg/mL Hygromycin-B (Thermo Fisher) over about two weeks until all untransfected cells have died and colonies have appeared in transfected cells. Stably integrated cells were maintained in RPMI, 10% FBS buffer (v/v), 1 mM sodium pyruvate, 10 mM HEPES, 2 mM glutamine and 50 μM β-mercaptoethanol, 25 μg/mL Hygromycin-B. HEK293 cells (ATCC, # CRL-1573) were

grown in DMEM High Glucose media (Gibco) supplemented with 10% FBS. HCT-116 (ATCC, #CCL-247) cells were maintained in McCoy's 5A modified media (Gibco) supplemented with 10% FBS. Non-diabetic human islets were obtained from Prodo Labs (Irvine, CA) and cultured in supplemented Prodo Islet Medium (PIM(S) from Prodo Labs). All cells lines were maintained at 37°C with 5% CO_2.

RNA isolation, quantitative real-time PCR, and primers—INS-1 or isogenic IRE1α-overexpressing INS-1 cells were plated onto Poly-D-Lysine coated tissue culture plate and grown for 48 hrs. Inhibitors or DMSO were added to the media and incubated for 1 hr at 37 °C with 5% CO_2 prior to addition of ER stress agents or Dox as indicated. Islets were pretreated with either DMSO, **PAIR1**, or **KIRA9** for 2 hrs at 37°C with 5% CO_2 followed by treatment with 2.5 mM DTT for 2 hours. RNA was isolated from whole cells using either QIAGEN RNeasy Mini kits or Trizol (Invitrogen) and reverse transcribed as above to obtain total cDNA. Then, XBP-1 primers were used to amplify an XBP-1 amplicon spanning the 26 nt intron from the cDNA samples in a regular 3-step PCR. Thermal cycles were: 5 min at 95 °C, 30 cycles of 30 s at 95 °C, 30 s at 60 °C, and 1 min at 72 °C, followed by 72 °C for 15 min, and hold at 4 °C. Primers used for XBP-1 mRNA splicing were as follows: sense primer XBP1.3S (5'-AAACAGAGTAGCACAGACTGC-3') and antisense primer XBP1.2AS (5'-GGATCTCTAAGACTAGAGGCTTGGTG-3'). PCR fragments were then digested by PstI, resolved on 3% agarose gels, stained with EtBr and quantified by densitometry using ImageJ (NIH). For standard mRNA detection, generally 1 mg total RNA was reverse transcribed using the QuantiTect Reverse Transcription Kit (QIAGEN). For qPCR, we used SYBR green (QIAGEN) and StepOnePlus Real-Time PCR System (Applied Biosystems). Thermal cycles were: 5 min at 95 °C, 40 cycles of 15 sec at 95 °C, 30 sec at 60 °C. Gene expression levels were normalized to Beta Actin. Primers used for qPCR of RIDD targets were as follows: Beta Actin Fwd: 5'-GCAAATGCTTCTAGGCGGAC-3', Beta Actin Rev: 5'AAGAAAGGGTGTAAAACGCAGC-3', Insulin 1 Fwd: 5'-GTCCTCTGGGAGCCCAAG-3', Insulin 1 Rev: 5'-ACAGAGCCTCCACCAGG-3', Insulin 2 Fwd: 5'-ATCCTCTGGGAGCCCCGC-3', Insulin 2 Rev: 5'-AGAGAGCTTCCACCAAG-3', Blos1 Fwd: 5'-CAAGGAGCTGCAGGAGAAGA-3', and Blos1 Rev: 5'-GCCTGGTTGAAGTTCTCCAC-3'.

Annexin-V staining

For assaying apoptosis by Annexin V staining, cells were plated in 12-well plates overnight. Cells were then treated with various reagents for indicated time periods. On the day of flow cytometry analysis, cells were trypsinized and washed in PBS and resuspended in Annexin V binding buffer with Annexin-V FITC (BD Pharmingen™). Flow cytometry was performed on a BD Biosciences FACSDiva.

RNA sequencing

RNA isolation and preparation—Isogenic IRE1α-overexpressing INS-1 cells were pretreated with inhibitors for 1 hr followed by addition of Dox 5 ng/ml for 4 hr or 24 hr. All conditions for RNA-Seq analysis were performed in three biological replicates. RNA was isolated from whole cells using Qiagen RNeasy with gDNA eliminator kit. RNA purity was determined using a NanaPhotometer spectrometer (IMPLEN, CA, USA). RNA integrity and

quantitation were assessed using the RNA Nano 6000 Assay Kit of the Bioanalyzer 2100 system (Agilent Technologies, CA, USA).

Library preparation—Library preparation for RNA-Seq was performed by Novogene. A total amount of 1 μg RNA per sample was used as input material for the RNA sample preparations. Sequencing libraries were generated using NEBNext® Ultra™ RNA Library Prep Kit for Illumina® (NEB, USA) following manufacturer's recommendations and index codes were added to attribute sequences to each sample. Briefly, mRNA was purified from total RNA using poly-T oligo-attached magnetic beads. Fragmentation was carried out using divalent cations under elevated temperature in NEBNext First Strand Synthesis Reaction Buffer (5X). First strand cDNA was synthesized using random hexamer primer and MMuLV Reverse Transcriptase (RNase H). Second strand cDNA synthesis was subsequently performed using DNA Polymerase I and RNase H. Remaining overhangs were converted into blunt ends via exonuclease/polymerase activities. After adenylation of 3' ends of DNA fragments, NEBNext Adaptor with hairpin loop structure were ligated to prepare for hybridization. In order to select cDNA fragments of preferentially 150–200 bp in length, the library fragments were purified with AMPure XP system (Beckman Coulter, Beverly, USA). Then 3 μL USER Enzyme (NEB, USA) was used with size-selected, adaptor-ligated cDNA at 37 °C for 15 min followed by 5 min at 95 °C before PCR. Then PCR was performed with Phusion High-Fidelity DNA polymerase, Universal PCR primers and Index (X) Primer. Finally, PCR products were purified (AMPure XP system) and library quality was assessed on the Agilent Bioanalyzer 2100 system.

Clustering and sequencing—The clustering of the index-coded samples was performed on a cBot Cluster Generation System using PE Cluster Kit cBot-HS (Illumina) according to the manufacturer's instructions. After cluster generation, the library preparations were sequenced on an Illumina platform and 125 bp/150 bp paired-end reads were generated.

Quality control and genome mapping—Raw data (raw reads) of fastq format were firstly processed using Novogene perl scripts. In this step, clean data (clean reads) were obtained by removing reads containing adapter, reads containing ploy-N and low quality reads from raw data. At the same time, Q20, Q30 and GC content the clean data were calculated. All the downstream analyses were based on the clean data with high quality. Reference genome and gene model annotation files were downloaded from genome website directly. Index of the reference genome was built using hisat2 2.1.0 and paired-end clean reads were aligned to the reference genome using HISAT2.

Quantification of gene expression level—HTSeq v0.6.1 was used to count the reads numbers mapped to each gene. And then FPKM of each gene was calculated based on the length of the gene and reads count mapped to this gene. FPKM, expected number of Fragments Per Kilobase of transcript sequence per millions base pairs sequenced, considers the effect of sequencing depth and gene length for the reads count at the same time, and is currently the most commonly used method for estimating gene expression levels.[48]

Differential expression analysis—Differential expression analysis of two conditions/ groups (three biological replicates per condition) was performed using the DESeq R

package (1.18.0). DESeq provide statistical routines for determining differential expression in digital gene expression data using a model based on the negative binomial distribution. The resulting P-values were adjusted using the Benjamini and Hochberg's approach for controlling the false discovery rate. Genes with an adjusted P-value < 0.05 found by DESeq were assigned as differentially expressed

GO and KEGG enrichment analysis of differentially expressed genes—Gene Ontology (GO) enrichment analysis of differentially expressed genes was implemented by the GOseq R package, in which gene length bias was corrected. GO terms with corrected P-value less than 0.05 were considered significantly enriched by differential expressed genes. KEGG is a database resource for understanding high-level functions and utilities of the biological system, such as the cell, the organism and the ecosystem, from molecular-level information, especially large-scale molecular datasets generated by genome sequencing and other high-through put experimental technologies (http://www.genome.jp/kegg/). We used KOBAS software to test the statistical enrichment of differential expression genes in KEGG pathways.

Splenocyte isolation and plasma cell differentiation—Splenocytes were isolated from C57BL/6 mice into single cell suspension in complete media: RPMI 1640, L-glutamine (Corning-Gibco), penicillin/streptomycin L-glutamine (Life Technologies), 10 mM HEPES buffer (Life Technologies), non-essential amino acids (Life Technologies), 1 mM sodium pyruvate (Life Technologies), 55 mM 2-mercaptoethanol (Gibco), and 10% heat inactivated fetal bovine serum (Omega Scientific). Red blood cells were lysed with ammonium chloride potassium buffer. Cells were loaded with CellTrace Violet (CTV; Invitrogen) per the manufacturer's instructions except at 5×10^6 cells/ml rather than 1×10^6 cells/ml. Splenocytes were plated at 2.5×10^5 cells/well in a 96-well round bottom plate in complete media. The splenocytes were treated with or without 1 μg/ml LPS 026:b6 (Sigma). Two-fold serial dilutions of IRE1α inhibitors (20 μM-1.25 μM) were prepared in DMSO and added to the LPS treated cells at a final dilution of 1:2000. The splenocytes were incubated for three days in a 37°C, 5% CO_2 humidified chamber before collection and staining for flow cytometry.

Flow cytometry—Cells from the plasma cell assay were collected in a 96-well plate and washed with PBS followed by staining with LIVE/DEAD Fixable Near-IR Dead Cell Stain kit (Invitrogen). Reagent was reconstituted as per manufacturer's instructions, diluted 1:1000 in PBS, and cells were stained in 100 μL on ice for 20 minutes. The cells were then washed with FACS buffer, PBS (Corning), 2 mM EDTA and 2% heat inactivated fetal bovine serum (Omega Scientific). The cells were then stained with 50 μL antibody cocktail consisting of anti-CD19 (BioLegend), anti-CD45R (BD Pharmingen), and anti-CD138 (BioLegend) in FACS buffer on ice for 15 minutes. Cells were washed twice with 200 μL FACS buffer. XBPIs staining was performed utilizing a Foxp3/transcription factor buffer set (eBioscience) per the manufacturer's instructions in conjunction with Alexa Fluor 647 anti-XBPIs (BD Biosciences). Cells were resuspended in FACS buffer and combined with an equal volume of 4% paraformaldehyde with 5000 Countbright Absolute Counting Beads

(Thermofisher). Stained cells were analyzed on a Fortessa (Becton Dickinson). Division index and data analyses were performed using FlowJo (v10) software (Treestar Inc.).

ELISA for secreted IgM—Media supernatants from the in vitro plasma cell differentiation assay were measured for secreted IgM by ELISA. 96-well plates (Costar, #3690) were coated with 1 μg/ml goat anti-IgM (Southern Biotech, #1020–01) in PBS. Wash buffer (PBS with 0.05% Tween-20 (v/v)) was used for all washing steps and blocked with PBS-BB (PBS without Ca^{2+}/Mg^{2+}, 1% BSA (w/v), 0.05% Tween-20(v/v)). Supernatants from LPS stimulated samples were diluted (1:100) and media only samples were diluted (1:10) in PBS-BB. IgM standard (Southern Biotech, #0101–01) was prepared in a 2-fold serial dilution in PBS-BB. IgM was detected with Goat anti-IgM-HRP (Southern Biotech, #1020–05) diluted (1:3000) in PBS-BB. ELISA plates were developed with TMB (Sigma) and stopped with 1 N sulfuric acid. Absorbance was measured at 450 nm using spectrophotometer (Spectramax M5, Molecular Devices). Sample IgM concentration values were calculated with SoftMaxPro v7 software.

Synthesis of IRE1α modulators

See Supplementary Information and Note.

Statistical analysis

Quantitative data are presented as mean ± standard error of the mean (SEM), as specified in the figure legends. Information regarding the number of replicates or samples and statistical analyses are described in the corresponding figure and table legends.
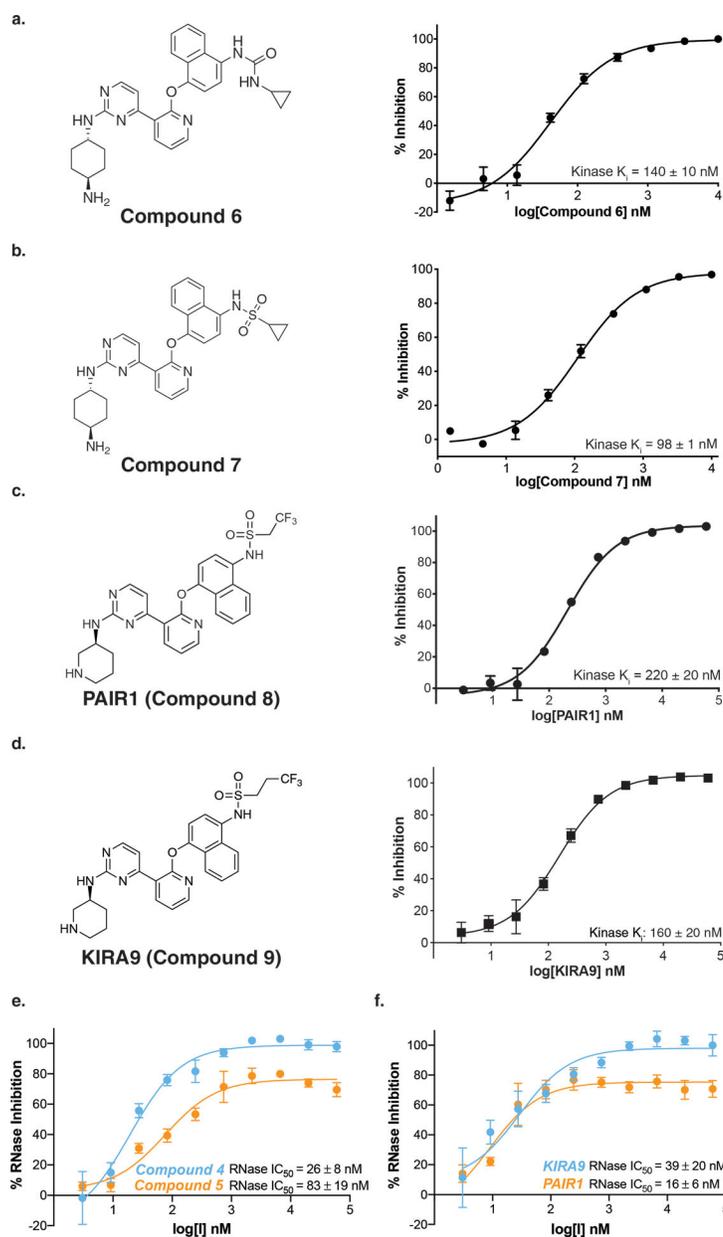
Extended Data
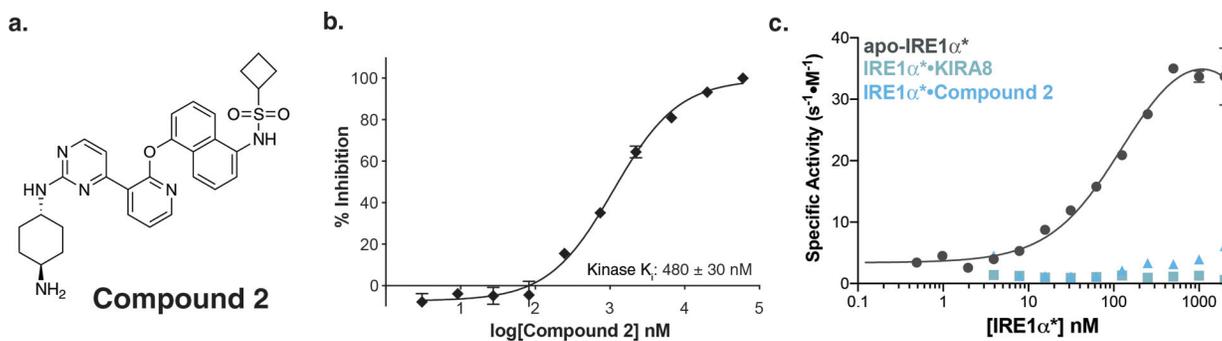
Extended Data Fig. 1. KIRAs monomerize IRE1α*
(a) Chemical structure of compound **2**. (b) Inhibition of IRE1α*'s kinase activity by compound **2** (K_i = 480 nM). Data points shown are the mean of n=3 independent experiments ± SEM. (c) K_{dimer} curve of the IRE1α*-compound **2** complex (*teal*). K_{dimer} curves of *apo* IRE1α* (dark gray) and the IRE1α*-KIRA8 complex (*light blue*) from Fig. 1e are shown for comparison. Data points shown are the mean of n=3 independent experiments ± SEM.
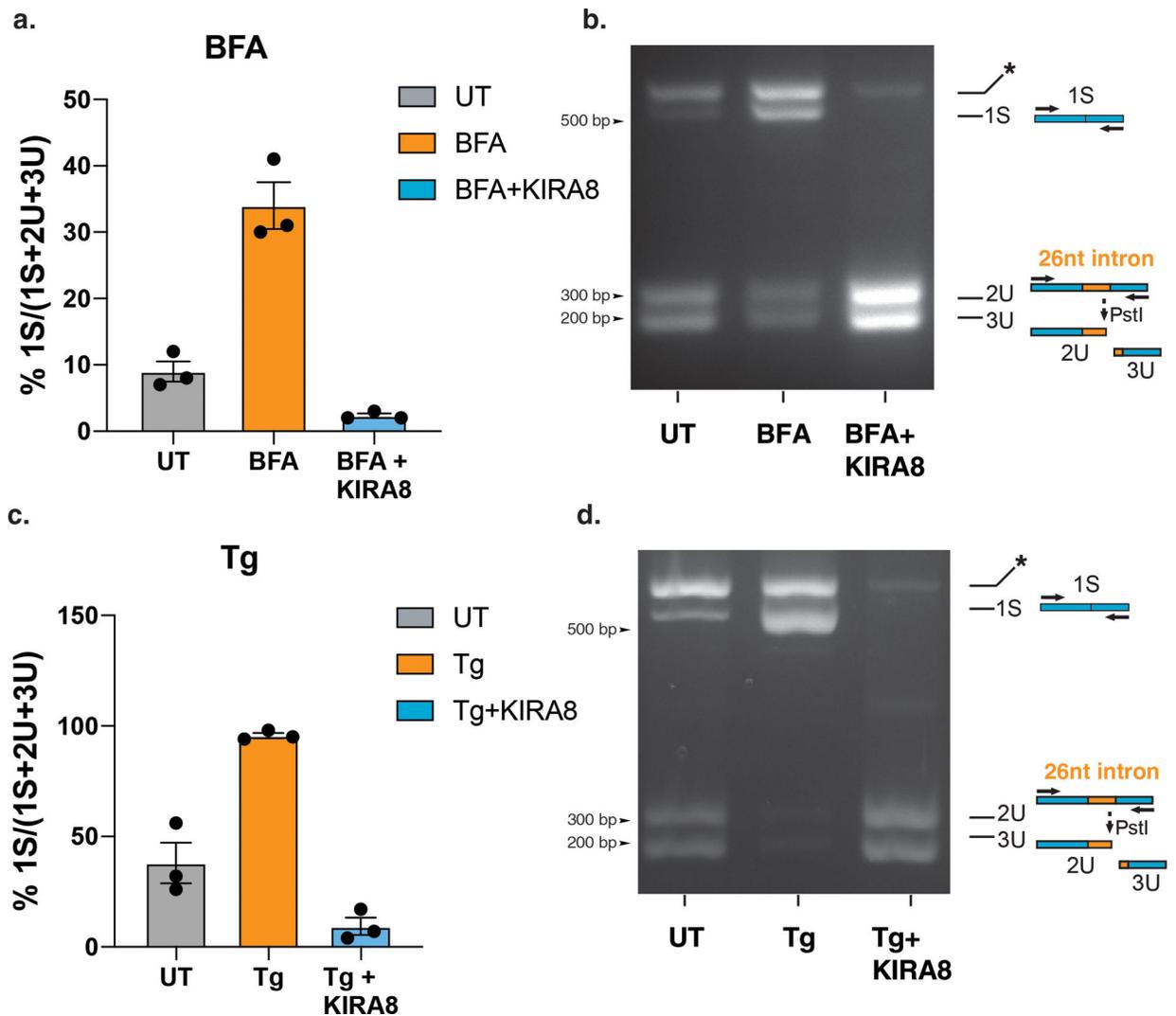
Extended Data Fig. 2. KIRA8 completely suppresses XBP1 splicing in ER-stressed INS-1 cells
a) Quantification of spliced XBP1 in untreated INS-1 cells and INS-1 cells treated with brefeldin A (BFA) or BFA and KIRA8. Values shown are the mean of n=3 biologically independent samples ± SEM. (b) Representative example of an EtBr-stained agarose gel of XBP1 cDNA amplicons from INS-1 cells subjected to the conditions described in (a). (c) Quantification of spliced XBP1 in untreated INS-1 cells and INS-1 cells treated with thapsigargin (Tg) or Tg and KIRA8. Values shown are the mean of n=3 biologically independent samples ± SEM. (d) Representative example of an EtBr-stained agarose gel of XBP1 cDNA amplicons from INS-1 cells subjected to the conditions described in (c).

Extended Data Fig. 3. Structurally-related PAIRs and KIRAs

(a) Chemical structure of (*left*) and inhibition of IRE1α*'s kinase activity (*right*, K_i = 140 nM) by compound **6**. (b) Chemical structure of (*left*) and inhibition of IRE1α*'s kinase activity (*right*, K_i = 98 nM) by compound **7**. (c) Chemical structure of (*left*) and inhibition of IRE1α*'s kinase activity (*right*, K_i = 220 nM) by compound **8** (PAIR1). (d) Chemical structure of (*left*) and inhibition of IRE1α*'s kinase activity (*right*, K_i = 160 nM) by compound **9** (KIRA9). Inhibition of IRE1α*'s RNase activity by (e) compounds **4** and **5**, and (f) PAIR1 and KIRA9. All data points shown are the mean of n=3 independent experiments ± SEM.
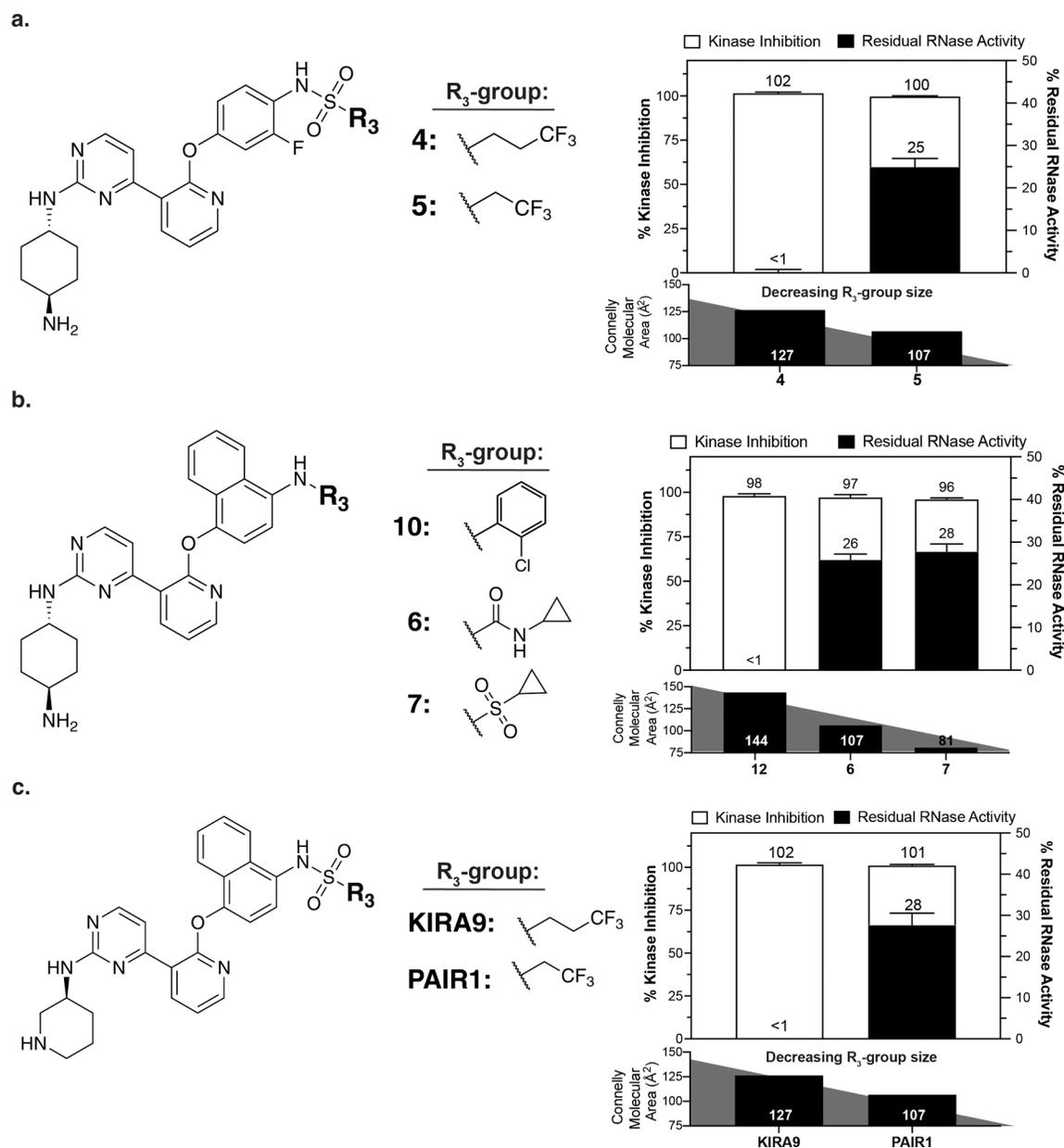
Extended Data Fig. 4. Partial antagonism of RNase activity is directly related to R₃-group size

Three-way correlation of kinase inhibition (a proxy for ATP-binding site occupancy), residual RNase activity, and R_3-group size measured as Connelly molecular surface area ($Å^2$) from matched inhibitor sets: (a) **4** and **5**, (b) **10** (a previously described KIRA), **6**, **7**, and (c) KIRA9 and PAIR1. Kinase inhibition and residual RNase activity are shown as the mean of n=3 independent experiments ± SEM. *Note: values are also shown in* Fig. 2f.
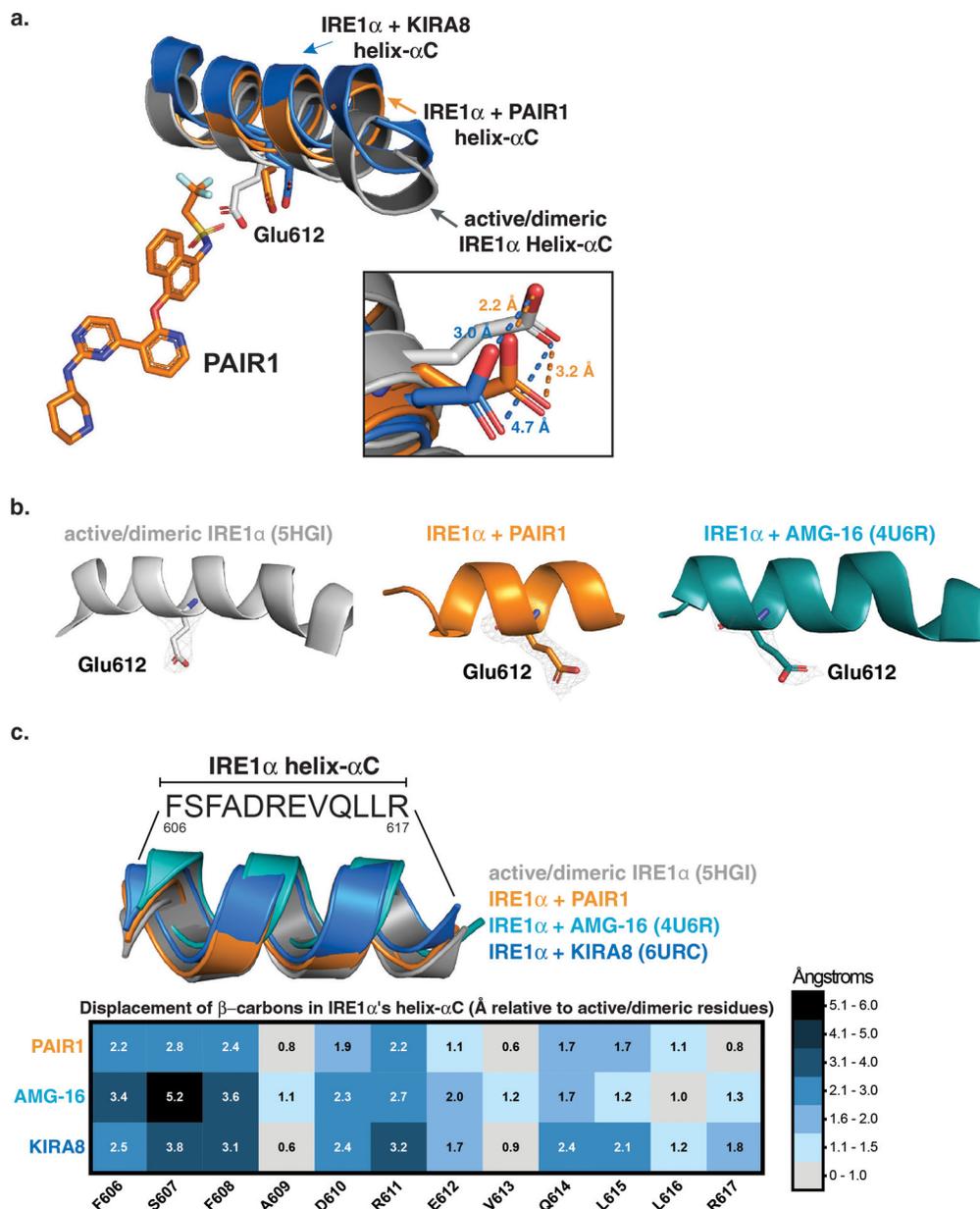
**Extended Data Fig. 5. PAIR1 stabilizes an intermediately displaced helix-αC**

(a) Superimposition of the helix-αCs of active IRE1α* (*gray*, PDB: 5HGI) with the PAIR1-IRE1α* complex (*orange*), and the KIRA8-IRE1α* complex (*blue*, PDB: 6URC). Inset displays the displacement of Glu612 within the helix-αC relative to active IRE1α* (*gray*, PDB: 5HGI). (b) 2Fo-Fc electron density maps of Glu612 from active IRE1α* (*gray*, PDB: 5HGI), PAIR1-IRE1α* (*orange*), and AMG-16-IRE1α* (*teal*, PDB: 4U6R), contoured to 1.0σ shown as gray isomesh, revealing strong electron density for Glu612, making it a suitable residue to measure approximate helix-αC movement. (c) Displacement of β-carbons from helix-αC residues (606–617) from co-crystal structures of IRE1α* with PAIR1 (orange), AMG-16 (teal, PDB: 4U6R), and KIRA8 (blue, PDB: 6URC) relative to active IRE1α* (*gray*, PDB: 5HGI).
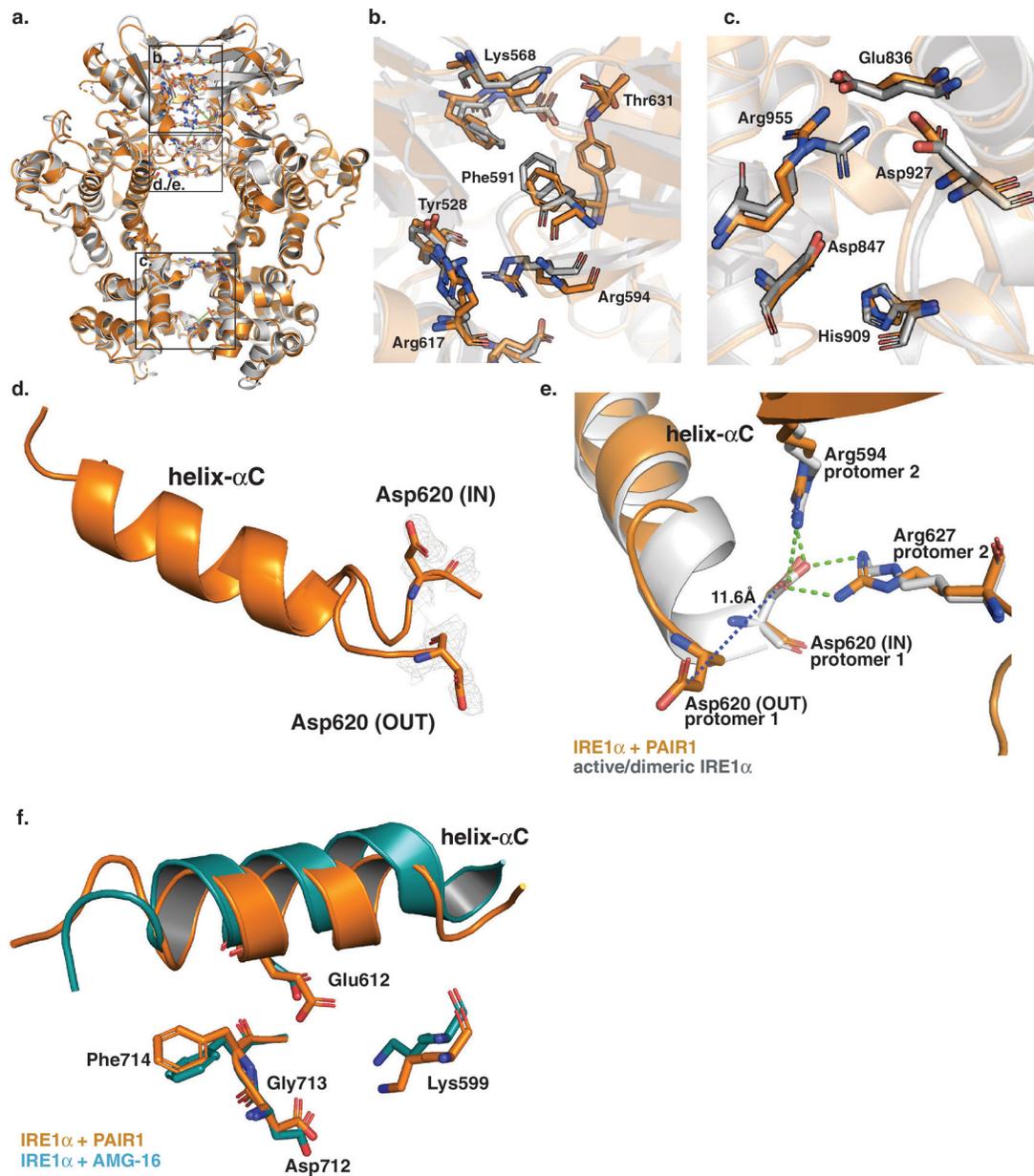
Extended Data Fig. 6. The PAIR1-bound IRE1α* dimer interface is partially disrupted through Asp 620 displacement

(a) Superimposition of the active IRE1α* (*gray*, PDB: 5HGI) and PAIR1-IRE1α* complex (*orange*) dimers. (b,c) Zoom-in views of the dimer interface contacts that are similar between active IRE1α* (*gray*, PDB: 5HGI) and the PAIR1-IRE1α* complex (*orange*) dimers. (d) 2Fo-Fc electron density maps of Asp620, contoured to 1.0σ shown as gray isomesh, reveal equal distribution of Asp620 between 'in" and "out" conformations. (e) Superimposition of dimer interface residue Asp620 from active IRE1α* (*gray*, PDB: 5HGI) and the PAIR1-IRE1α* complex (*orange*) shows that Asp620-IN is in a similar conformation as active IRE1α* and forms a salt bridge with the side-chains of Arg594 and Arg627 of the adjacent IRE1α* protomer. In the other conformation, Asp620-OUT, the side-chain of Asp620 is displaced 11.6 Å and can no longer form a salt bridge with

Arg594 and Arg627. This inter-dimer salt bridge between Asp620 and Arg594/Arg627 is essential for RNase active dimer formation and although Asp620 is found equally in conformations productive (Asp620-IN) and unproductive (Asp620-OUT) for RNase active dimer formation, the cumulative effect is partial disruption of the RNase active dimer interface. (f) Superimposition of kinase catalytic residues: K599, Glu612, and the DFG-motif (Asp712, Gly713, Phe714) from the PAIR1-IRE1α* complex (*orange*) and the AMG-16-IRE1α* complex (*teal*, PDB:4U6R) reveal that residues outside of the helix-αC (K599 and the DFG-motif) are in similar conformations, suggesting that differences in the pharmacology between PAIRs and KIRAs stems directly from helix-αC movement.
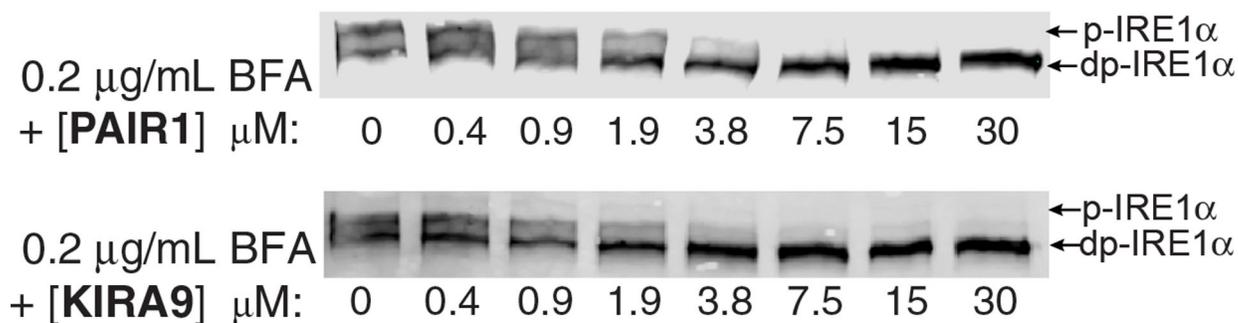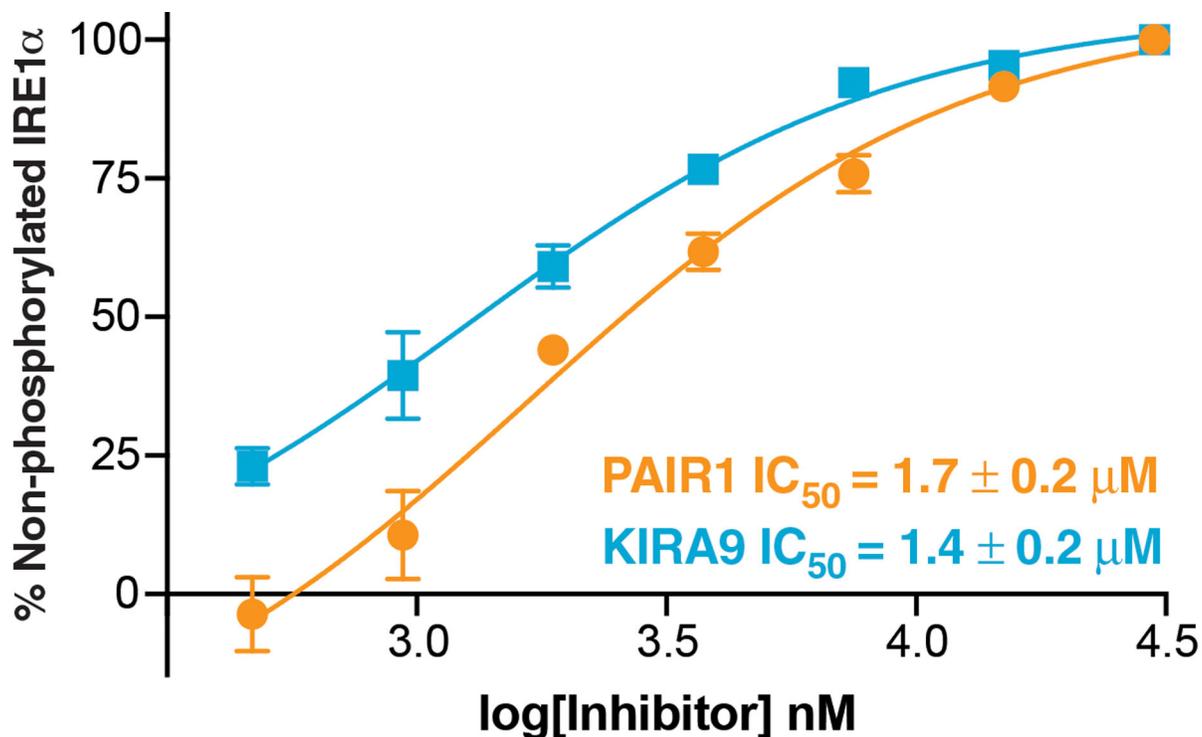
Extended Data Fig. 7. PAIR1 and KIRA9 equipotently block ER stress-induced IRE1α autophosphorylation

Immunoblots for total IRE1α (*bottom*) from INS-1 cells treated with various concentrations of PAIR1 or KIRA9 followed by the addition of 200 ng/μL Brefeldin-A (BFA) for 2 hours. Samples were subjected to phostag SDS-PAGE and % non-phosphorylated IRE1α (*top*) was

determined from the ratio of dephosphorylated IRE1α relative to total IRE1α. Values shown are the mean of n=3 biologically independent samples ± SEM.
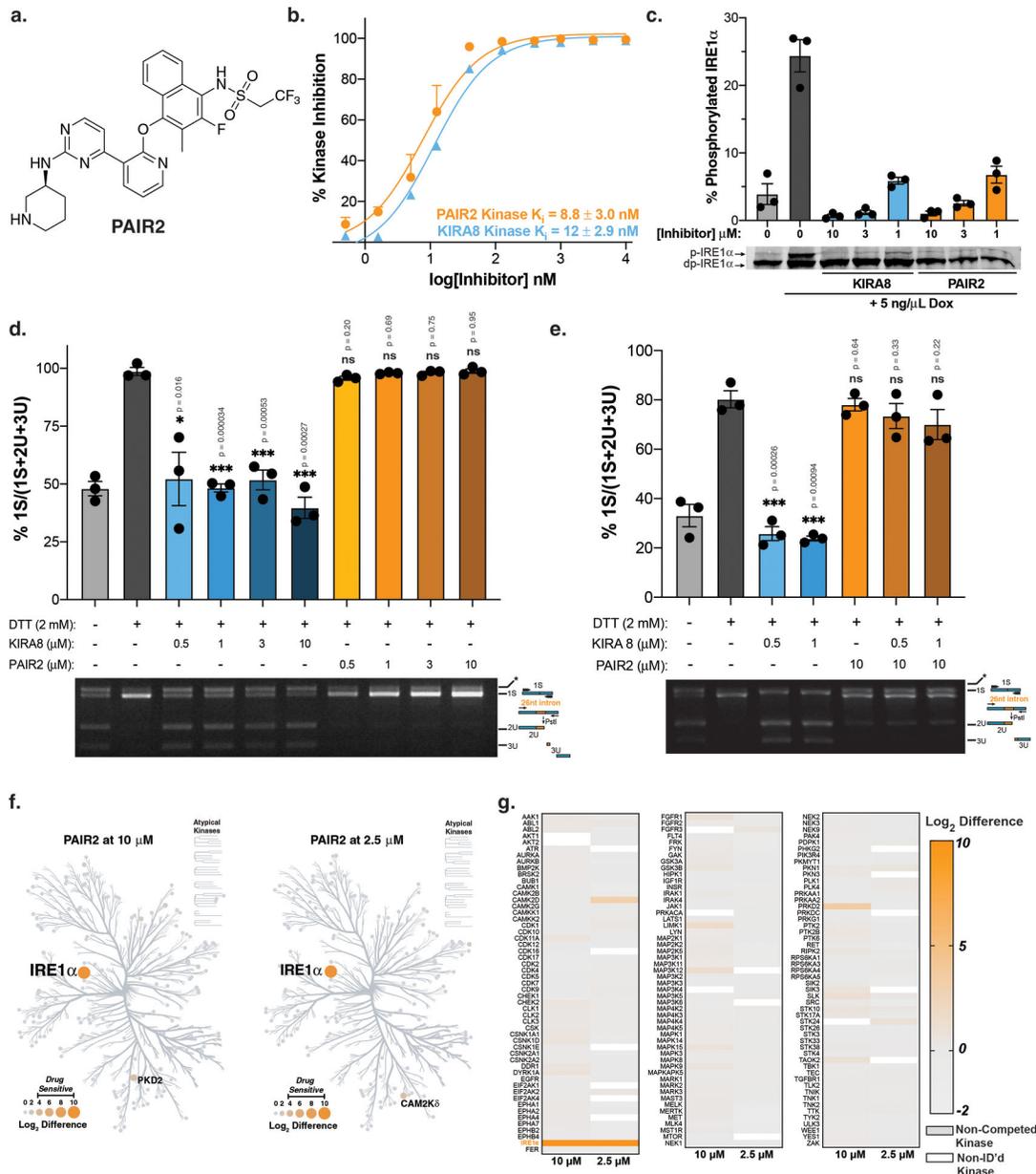
Extended Data Fig. 8. Characterization of the highly potent PAIR, PAIR2
(a) Chemical structure of PAIR2. (b) Inhibition of IRE1α*'s kinase activity by PAIR2 (K_i = 8.8 nM, values shown as the mean of n=3 independent experiments ± SEM) and KIRA8 (K_i = 12 nM, values shown as the mean of n=2 independent experiments). (c) Immunoblots for total IRE1α (*bottom*) from INS-1 cells treated with various concentrations of PAIR2 or KIRA8 followed by the addition of 5 ng/μL doxycycline (Dox) for 6 hours. Samples were subjected to phostag SDS-PAGE and % phosphorylated IRE1α (*top*) was determined from the ratio of phosphorylated IRE1α relative to total IRE1α. Values shown are the mean

of n=3 independent experiments ± SEM. (d) Percent spliced XBP1 (quantified from PstI-digested XBP1 cDNA amplicons) from INS-1 cells treated with DMSO, PAIR2, or KIRA8 (0.5, 1, 3, 10 μM) followed by the addition of 1,4-dithiothreitol (DTT) at 2 mM (*top*). Data shown are the mean of n=3 biologically independent samples ± SEM. A representative EtBr-stained agarose gel of XBP1 cDNA amplicons is shown below. (e) Percent spliced XBP1 (quantified from PstI-digested XBP1 cDNA amplicons) from INS-1 cells treated first with DMSO (lanes 1–4) or 10 μM PAIR2 (lanes 5–7) for 30 minutes followed by treatment with either DMSO (lanes 1, 2, and 5) or 0.5 or 1 μM KIRA8 (lanes 3, 4, 6, and 7) for 30 minutes followed by the addition of 1,4-dithiothreitol (DTT) at 2 mM (*top*). Data shown are the mean of n=3 biologically independent samples ± SEM. A representative EtBr-stained agarose gel of XBP1 cDNA amplicons is shown below. (f) Kinome selectivity of PAIR2 as determined by kinobead profiling. Kinases that were identified in the profiling experiment are shown with gray circles. Circle size and color have been scaled to the $\log_2$ ratio (difference in LFQ intensity) between DMSO and treatment with 10 and 2.5 μM of PAIR2 (mean of three and four replicates respectively). Kinases reported as being drug-sensitive ($\log_2$ Difference > 2) were also required to show significance from a two-sample T-test with FDR of 0.05. (g) Heat map displaying kinome selectivity from (f). P values calculated in (d), (e) are versus DTT treated cells and were determined using a two-tailed Student's t-test. *P < 0.05, **P < 0.01, ***P < 0.001.
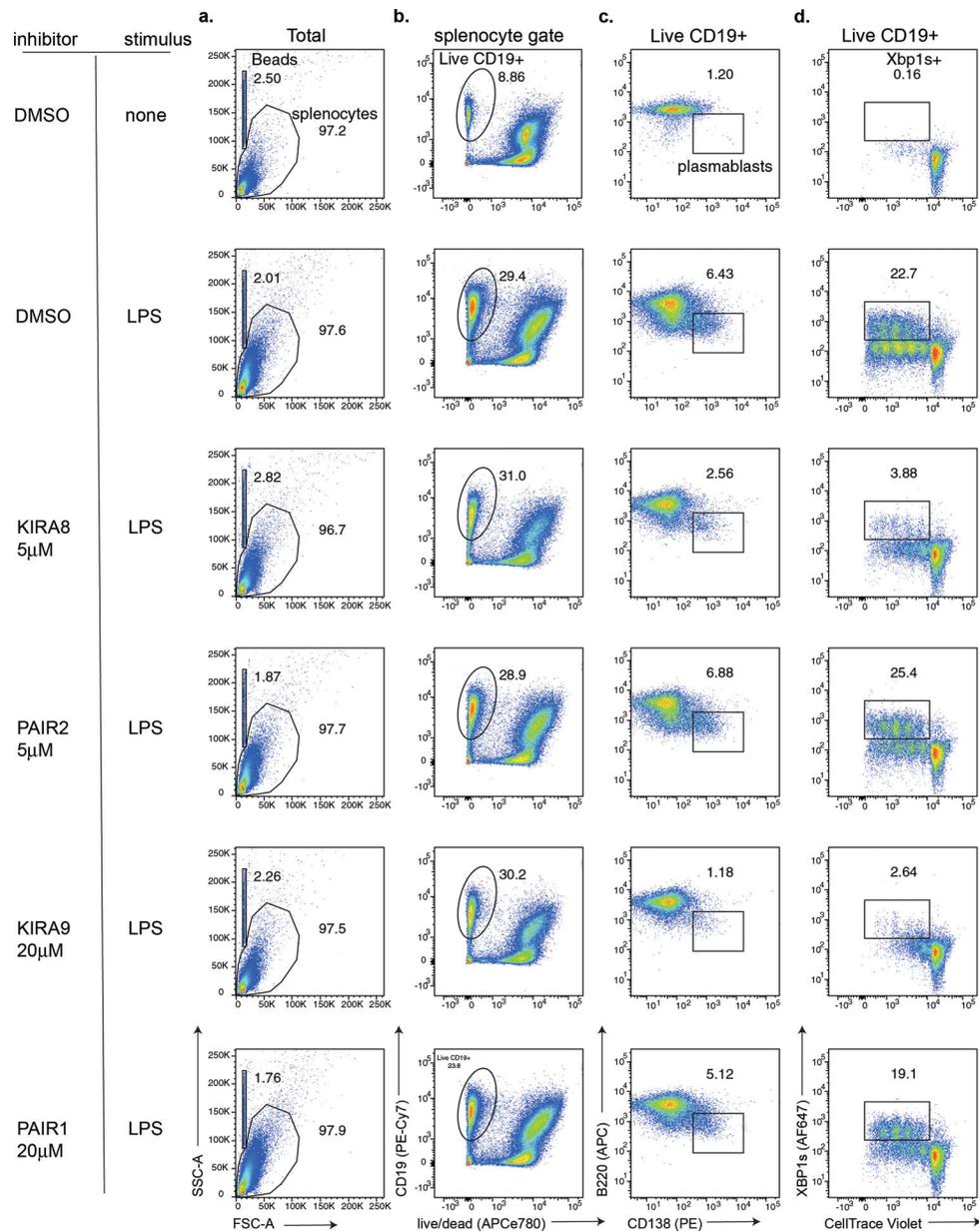
Extended Data Fig. 9. Flow cytometric analysis of lipopolysaccharide (LPS)-treated mouse splenocytes.

Mouse splenocytes were loaded with vital dye and subsequently cultured +/− 1 μg/mL LPS for three days in the presence or absence of KIRA8, KIRA9, PAIR1, or PAIR2 at noted concentrations. Following culture, cells were stained to detect surface marker expression and subsequently permeabilized to detect XBP1s intra-cellular expression. Samples were mixed with a fixed number of counting beads and collected by flow cytometry. Representative plots are displayed. (a) Splenocytes and beads were first gated on the basis of forward scatter (FSC) and side scatter (SSC) for the purpose of absolute quantification of cell number. (b) Live B-cells were then identified on the basis of CD19 expression and exclusion of live/dead dye. (c) Plasmablasts were identified as CD19+ cells with downregulation of B220 and upregulation of CD138 expression. (d) Plots depict vital dye dilution as a marker of cell

division and XBP1s+ gate. Corresponding quantification of these cell populations is shown in Fig. 6 and Extended Data Fig. 10.
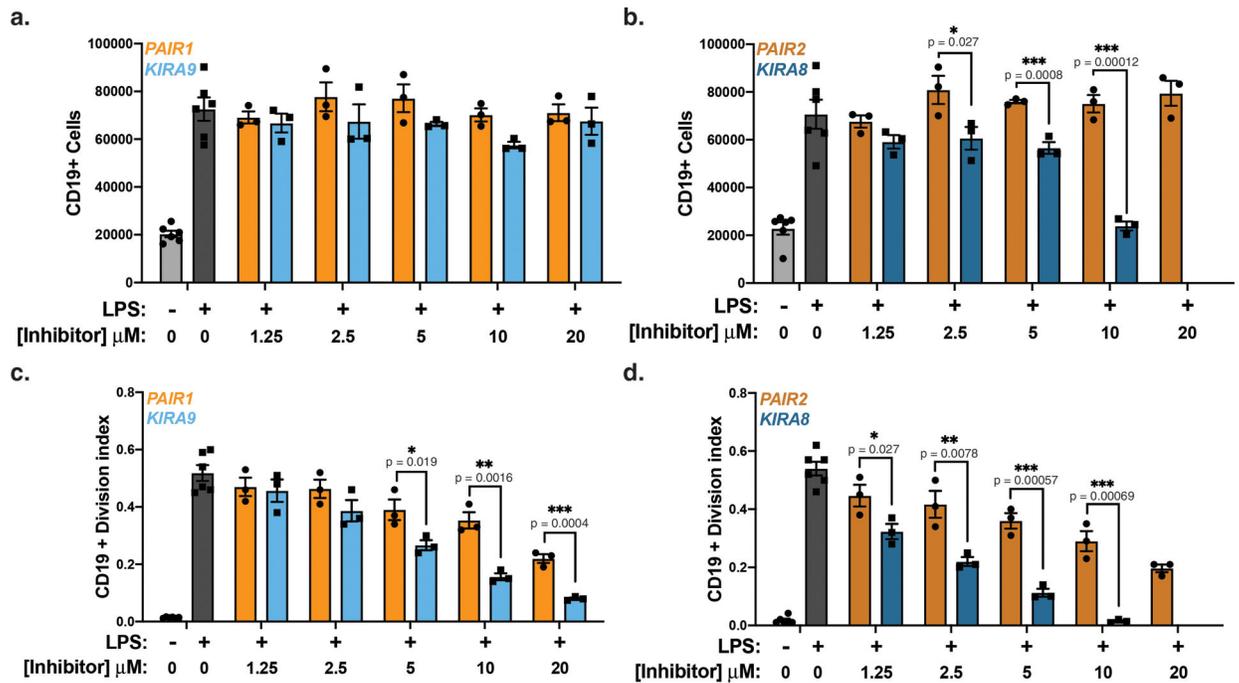
Extended Data Fig. 10. Effect of PAIRs and KIRAs on B-cell division

Quantification of CD19 positive cells following treatment of mouse splenocytes with 1 μg/mL LPS for three days in the presence or absence of various concentrations of (a) PAIR1 (*orange*) or KIRA9 (*teal*) or (b) PAIR2 *(dark orange)* or KIRA8 *(dark blue)* as gated in Extended Data Fig. 9. (c, d) Division index of CD19+ cells treated as in (a, b) was calculated via Flowjo on the basis of vital dye dilution (as shown in Extended Data Fig. 9). P values were calculated using one-tailed Student's t-test. *P < 0.033, **P < 0.002, ***P < 0.001. Data for 20 μM KIRA8 could not be generated due to cellular toxicity. All data shown are the mean of n=3 biologically independent samples ± SEM.

Supplementary Material

Refer to Web version on PubMed Central for supplementary material.

Acknowledgements:

Competing Interests Statement:

B.J.B., F.R.P, and D.J.M. are founders, equity holders, and consultants for OptiKIRA, LLC (Cleveland, OH), a biotech company founded on the treatment of ER-stress induced retinal degeneration—no company funding or chemical matter supported the work in this manuscript. J.Z serves on the SAB for Walking Fish Therapeutics.

Data Availability

Kinome selectivity data is provided in Supplementary Dataset 1. Coordinates and structure factors have been deposited in the Protein Data Bank under accession code: 7BMK. Cell line RNA-sequencing data has been deposited to the Gene Expression Omnibus[49] and are accessible through GEO Series accession number: GSE164496 (https://www.ncbi.nlm.nih.gov/geo/query/acc.cgi?acc=GSE164496). The KEGG database used in this study was acquired from http://www.genome.jp/kegg/. Raw data including unprocessed Western blots and agarose gels for Fig. 4, Fig. 5, Extended Data Fig. 2, Extended Data Fig. 7, and Extended Data Fig. 8 have been provided as source files.

References

1. Walter P, Ron D, The unfolded protein response: from stress pathway to homeostatic regulation. Science 334, 1081–1086 (2011). [PubMed: 22116877]

2. Hetz C, Papa FR, The Unfolded Protein Response and Cell Fate Control. Mol Cell 69, 169–181 (2018). [PubMed: 29107536]

3. Cox JS, Shamu CE, Walter P, Transcriptional induction of genes encoding endoplasmic reticulum resident proteins requires a transmembrane protein kinase. Cell 73, 1197–1206 (1993). [PubMed: 8513503]

4. Mori K, Ma W, Gething M-J, Sambrook J, A Transmembrane Protein with a cdc2+/CDC28-Related Kinase Activity Is Required for Signaling from the ER to the Nucleus. Cell 74, 743–756 (1993). [PubMed: 8358794]

5. Oakes SA, Papa FR, The role of endoplasmic reticulum stress in human pathology. Annual review of pathology 10, 173–194 (2015).

6. Han D et al. , IRE1alpha kinase activation modes control alternate endoribonuclease outputs to determine divergent cell fates. Cell 138, 562–575 (2009). [PubMed: 19665977]

7. Yoshida H, Matsui T, Yamamoto A, Okada T, Mori K, XBP1 mRNA is induced by ATF6 and spliced by IRE1 in response to ER stress to produce a highly active transcription factor. Cell 107, 881–891 (2001). [PubMed: 11779464]

8. Calfon M et al. , IRE1 couples endoplasmic reticulum load to secretory capacity by processing the XBP-1 mRNA. Nature 415, 92–96 (2002). [PubMed: 11780124]

9. Tirasophon W, Welihinda AA, Kaufman RJ, A stress response pathway from the endoplasmic reticulum to the nucleus requires a novel bifunctional protein kinase/endoribonuclease (Ire1p) in mammalian cells. Genes Dev 12, 1812–1824 (1998). [PubMed: 9637683]

10. Ghosh R et al. , Allosteric inhibition of the IRE1alpha RNase preserves cell viability and function during endoplasmic reticulum stress. Cell 158, 534–548 (2014). [PubMed: 25018104]

11. Hollien J, Weissman JS, Decay of endoplasmic reticulum-localized mRNAs during the unfolded protein response. Science 313, 104–107 (2006). [PubMed: 16825573]

12. Hollien J et al. , Regulated Ire1-dependent decay of messenger RNAs in mammalian cells. J Cell Biol 186, 323–331 (2009). [PubMed: 19651891]

13. Wang L et al. , Divergent allosteric control of the IRE1alpha endoribonuclease using kinase inhibitors. Nat Chem Biol 8, 982–989 (2012). [PubMed: 23086298]

14. Feldman HC et al. , Structural and Functional Analysis of the Allosteric Inhibition of IRE1alpha with ATP-Competitive Ligands. ACS Chem Biol 11, 2195–2205 (2016). [PubMed: 27227314]

15. Mendez AS et al. , Endoplasmic reticulum stress-independent activation of unfolded protein response kinases by a small molecule ATP-mimic. Elife 4, e05434 (2015).

16. Ferri E et al. , Activation of the IRE1 RNase through remodeling of the kinase front pocket by ATP-competitive ligands. Nat Commun 11, 6387 (2020). [PubMed: 33318494]

17. Lee KP et al. , Structure of the dual enzyme Ire1 reveals the basis for catalysis and regulation in nonconventional RNA splicing. Cell 132, 89–100 (2008). [PubMed: 18191223]

18. Korennykh AV et al. , Cofactor-mediated conformational control in the bifunctional kinase/RNase Ire1. BMC Biol 9, 48 (2011). [PubMed: 21729334]

19. Prischi F, Nowak PR, Carrara M, Ali MM, Phosphoregulation of Ire1 RNase splicing activity. Nature communications 5, 3554 (2014).

20. Maly DJ, Papa FR, Druggable sensors of the unfolded protein response. Nat Chem Biol 10, 892–901 (2014). [PubMed: 25325700]

21. Harrington PE et al. , Unfolded Protein Response in Cancer: IRE1alpha Inhibition by Selective Kinase Ligands Does Not Impair Tumor Cell Viability. ACS Med Chem Lett 6, 68–72 (2015). [PubMed: 25589933]

22. Sanches M et al. Structure and mechanism of action of the hydroxy–aryl–aldehyde class of IRE1 endoribonuclease inhibitors. Nat. Commun 5, 4202 (2014). [PubMed: 25164867]

23. Bantscheff M et al. , Quantitative chemical proteomics reveals mechanisms of action of clinical ABL kinase inhibitors. Nat Biotechnol 25, 1035–1044 (2007). [PubMed: 17721511]

24. Golkowski M et al. , Kinobead and Single-Shot LC-MS Profiling Identifies Selective PKD Inhibitors. Journal of Proteome Research 16, 1216–1227 (2017) [PubMed: 28102076]

25. Golkowski M et al. , Kinome chemoproteomics characterization of pyrrolo[3,4-c]pyrazoles as potent and selective inhibitors of glycogen synthase kinase 3. Mol Omics 14, 26–36 (2018). [PubMed: 29725679]

26. Jan CH, Williams CC, Weissman JS, Principles of ER cotranslational translocation revealed by proximity-specific ribosome profiling. Science 346, 1257521 (2014). [PubMed: 25378630]

27. Plumb R, Zhang ZR, Appathurai S, Mariappan M, A functional link between the co-translational protein translocation pathway and the UPR. Elife 4, e07426 (2015)

28. Lerner AG et al. , IRE1alpha induces thioredoxin-interacting protein to activate the NLRP3 inflammasome and promote programmed cell death under irremediable ER stress. Cell Metab 16, 250–264 (2012). [PubMed: 22883233]

29. Reimold AM et al. , Plasma cell differentiation requires the transcription factor XBP-1. Nature 412, 300–307 (2001). [PubMed: 11460154]

30. Iwakoshi NN et al. , Plasma cell differentiation and the unfolded protein response intersect at the transcription factor XBP-1. Nat Immunol 4, 321–329 (2003). [PubMed: 12612580]

31. Shaffer AL et al. , XBP1, downstream of Blimp-1, expands the secretory apparatus and other organelles, and increases protein synthesis in plasma cell differentiation. Immunity 21, 81–93 (2004). [PubMed: 15345222]

32. Tirosh B, Iwakoshi NN, Glimcher LH, Ploegh HL, XBP-1 specifically promotes IgM synthesis and secretion, but is dispensable for degradation of glycoproteins in primary B cells. J Exp Med 202, 505–516 (2005). [PubMed: 16103408]

33. Kawahara T, Yanagi H, Yura T, Mori K, Endoplasmic reticulum stress-induced mRNA splicing permits synthesis of transcription factor Hac1p/Ern4p that activates the unfolded protein response. Mol Biol Cell 8, 1845–1862 (1997). [PubMed: 9348528]

34. Cox JS, Walter P, A novel mechanism for regulating activity of a transcription factor that controls the unfolded protein response. Cell 87, 391–404 (1996). [PubMed: 8898193]

35. Kimmig P et al. , The unfolded protein response in fission yeast modulates stability of select mRNAs to maintain protein homeostasis. Elife 1, e00048 (2012). [PubMed: 23066505]

36. Papa FR, Zhang C, Shokat K, Walter P, Bypassing a kinase activity with an ATP-competitive drug. Science 302, 1533–1537 (2003). [PubMed: 14564015]

37. Tong M, Seeliger MA, Targeting conformational plasticity of protein kinases. ACS Chem Biol. 10:190–200 (2015). [PubMed: 25486330]

38. Jura N, Zhang X, Endres NF, Seeliger MA, Schindler T, Kuriyan J, Catalytic control in the EGF receptor and its connection to general kinase regulatory mechanisms. Mol. Cell 42: 9–22 (2011) [PubMed: 21474065]

39. Zhang K et al. , The unfolded protein response sensor IRE1alpha is required at 2 distinct steps in B cell lymphopoiesis. J Clin Invest 115, 268–281 (2005). [PubMed: 15690081]

40. Iwawaki T, Akai R, Yamanaka S, Kohno K, Function of IRE1 alpha in the placenta is essential for placental development and embryonic viability. Proc Natl Acad Sci U S A 106, 16657–16662 (2009). [PubMed: 19805353]

41. Morita S, A. S. et al. , Targeting ABL-IRE1α signaling spares ER-stressed pancreatic β-cells to reverse autoimmune diabetes Cell Metab. 25, 883–97 (2017) [PubMed: 28380378]

42. Sato H, Shiba Y, Tsuchiya Y, Saito M, Kohno K, 4μ8C Inhibits Insulin Secretion Independent of IRE1α RNase Activity. Cell Struct Funct 42, 61–70 (2017). [PubMed: 28321016]

43. Papandreou I et al. , Identification of an Ire1alpha endonuclease specific inhibitor with cytotoxic activity against human multiple myeloma. Blood 117, 1311–1314 (2011). [PubMed: 21081713]

44. Grandjean J, et al. , Pharmacologic IRE1/XBP1s activation confers targeted ER proteostasis reprogramming. Nat. Chem. Biol 16, 1052–1061 (2020) [PubMed: 32690944]

45. Yu Y, Smith M & Pieper R, A spinnable and automatable StageTip for high throughput peptide desalting and proteomics. Nature Protocol Exchange (2014).

46. Metz et al. , Coral: Clear and Customizable Visualization of Human Kinome Dat Cell Systems 7, 347–350 (2018) [PubMed: 30172842]

47. Qi L, Yang L & Chen H, Detecting and quantitating physiological endoplasmic reticulum stress. Methods in Enzymology 490, 137–146 (2011) [PubMed: 21266248]

48. Trapnell C et al. , Transcript assembly and quantification by RNA-seq reveals unannotated transcripts and isoform switching during cell differentiation. Nat. Biotechnol 28, 511–515 (2010) [PubMed: 20436464]

49. Edgar R, Domrachev M, Lash AE. Gene Expression Omnibus: NCBI gene expression and hybridization array data repository Nucleic Acids Res. 30, 207–10 (2002) [PubMed: 11752295]

Author Manuscript
Author Manuscript
Author Manuscript
Author Manuscript
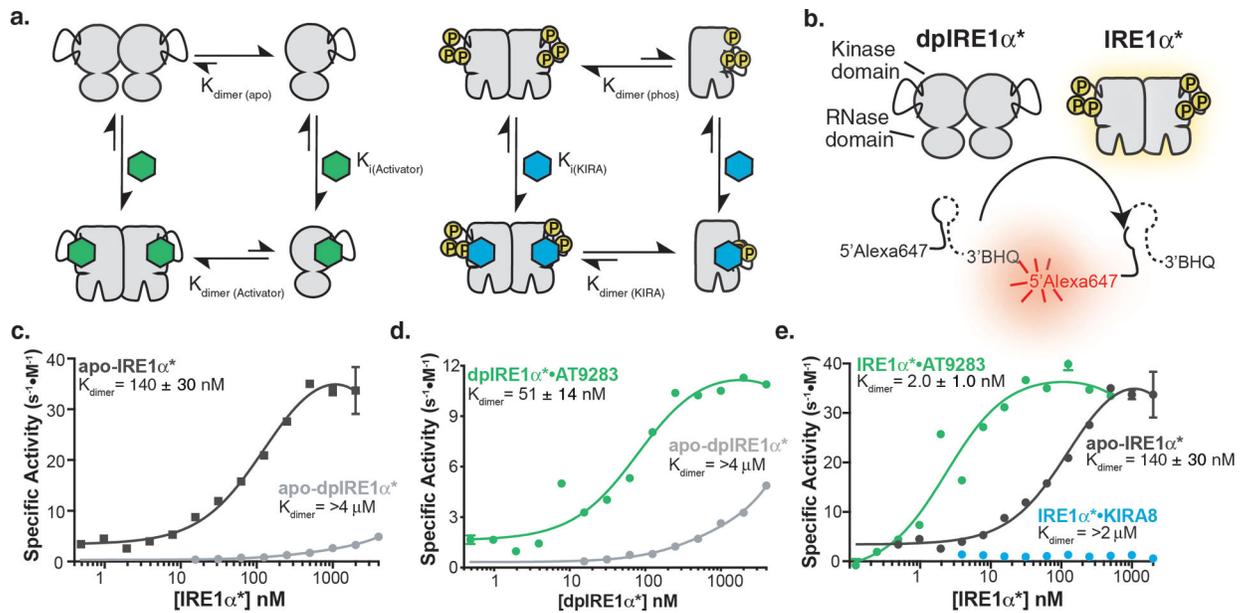
Figure 1. IRE1α dimerization is modulated by ATP-binding site occupancy

(a) Model of how ATP-competitive inhibitors affect the oligomerization state of different phosphorylation states of IRE1α. (b) Schematic of the recombinant constructs IRE1α* and dpIRE1α* (*top)*, which consist of the cytosolic kinase and RNase domains of IRE1α, and the *in vitro* XBP1 mini-substrate cleavage assay (*bottom*). (c) Dimerization affinity (K_{dimer}) curves for *apo*-IRE1α* (*dark gray*) and *apo*-dpIRE1α* (*light gray*). Data points shown are the mean of n=3 independent experiments ± SEM. (d). K_{dimer} curve for the dpIRE1α*-AT9283 complex (*green*). Data points shown are the mean of n=3 independent experiments ± SEM. The K_{dimer} curve of *apo*-dpIRE1α* (light gray) from Fig. 1c is shown for comparison. (e) K_{dimer} curves for the IRE1α*-AT9283 (*green*) and IRE1α*-KIRA8 (*blue*) complexes. Data points shown are shown as the mean of n=3 independent experiments ± SEM. The K_{dimer} curve of *apo*-IRE1α* (*dark gray*) from Fig. 1c is shown for comparison.
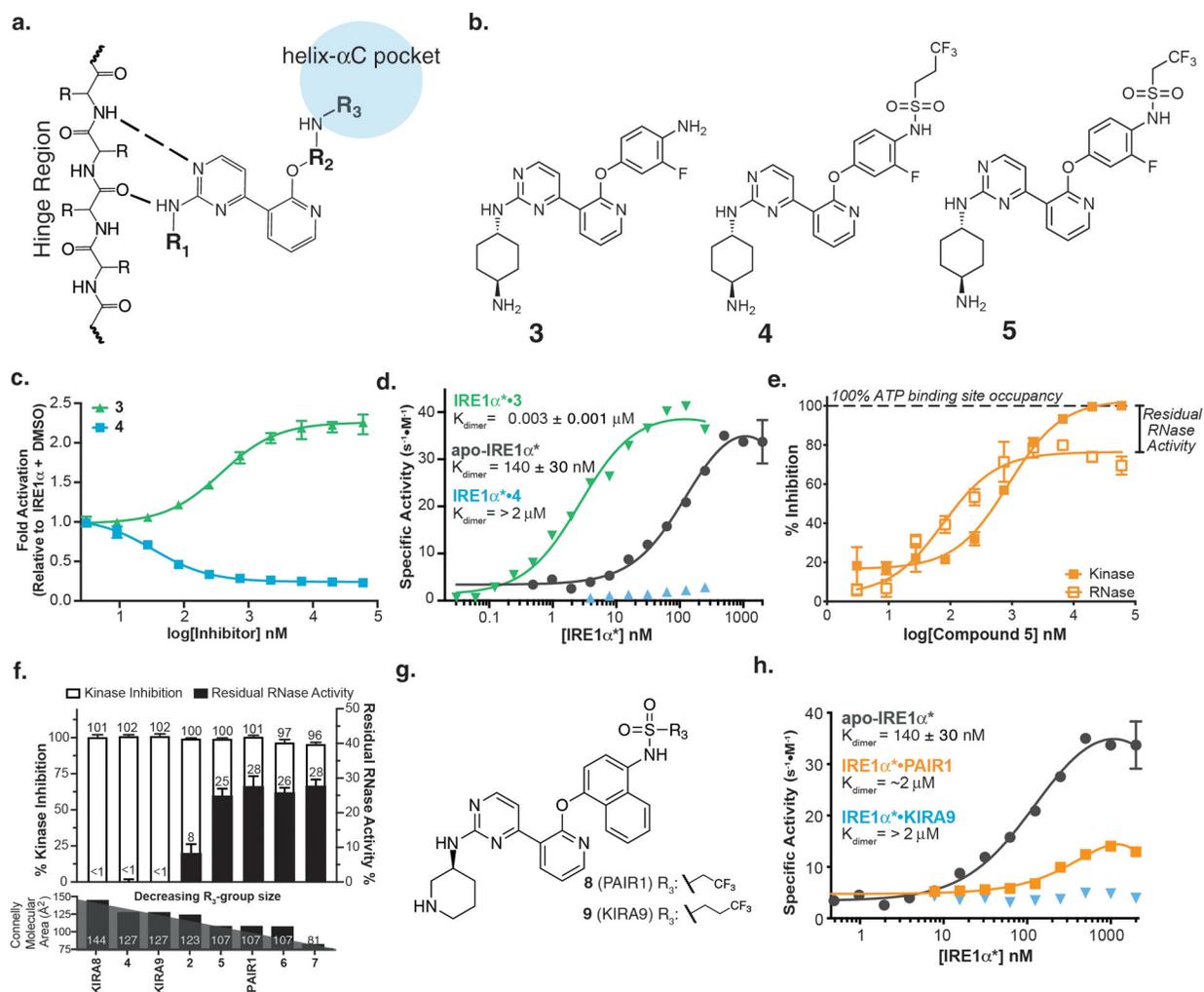
Figure 2. Partial antagonists of IRE1α's RNase activity

(a) Proposed binding mode of the pyridine-pyrimidine scaffold with IRE1α's ATP-binding site. Structural elements that are varied in our study are labeled as R_1, R_2, or R_3. (b) Structures of compounds **3-5**. (c) RNase activities of IRE1α* under varying concentrations of **3** and **4** relative to *apo*-IRE1α*. Data shown are the mean of n=3 independent experiments ± SEM. (d) K_{dimer} curves for the IRE1α*–**3** (*green*) and IRE1α*–**4** (*blue*) complexes. Values shown are mean of n=3 independent experiments ± SEM. The K_{dimer} curve of *apo*-IRE1α* (*dark gray*) from Fig. 1c is shown for comparison. (e) The kinase and RNase activities of IRE1α* under varying concentrations of **5**. IRE1α* retains ~20% of its RNase activity (residual activity) at full ATP-binding site occupancy. Data shown are the mean of n=3 independent experiments ± SEM. (f) Three-way correlation of kinase inhibition (a proxy for ATP-binding site occupancy), residual RNase activity, and R_3-group size measured as Connelly molecular surface area (Å^2). Kinase inhibition and residual RNase activity are shown as the mean of n=3 independent experiments ± SEM. (g) Structures of compounds PAIR1 and KIRA9. (h) K_{dimer} curves for the IRE1α*-PAIR1 (*orange*) and IRE1α*-KIRA9 (*blue*) complexes. Values shown are the mean of n=3 independent experiments ± SEM.
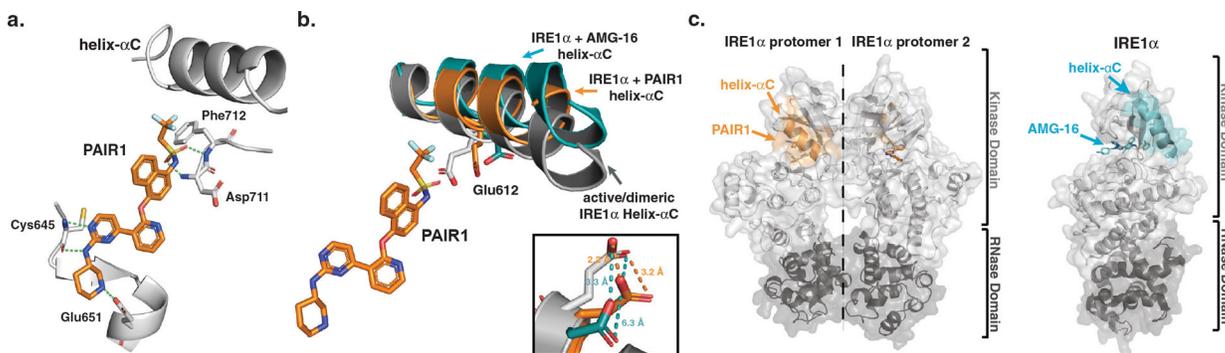
Figure 3. Co-crystal structure of the IRE1α-PAIR1 complex

(a) Interactions of PAIR1 with the ATP-binding site of and IRE1α. Key interactions (*dashed green lines*) between PAIR1 (*orange sticks*) and IRE1α are highlighted. Interacting residues are shown as gray sticks. (b) Superimposition of the helix-αCs of the IRE1α-PAIR1 (*orange*) and IRE1α-AMG-16 (*teal*, PDB: 4U6R) complexes and active IRE1α (*gray*). Inset displays the displacement of Glu612 within the helix-αC relative to active IRE1α* (*gray*, PDB: 5HGI). (c) Global structure of the IRE1α-PAIR1 *(left)* and IRE1α-AMG-16 *(right)* complexes. PAIR1–bound IRE1α crystallizes as a back-to-back dimer (the two-fold symmetry axis is denoted by a dashed line) while AMG-16-bound IRE1α crystallizes as a monomer. Each protomer contains a kinase domain (*light gray*) and an RNase domain (*dark gray*).
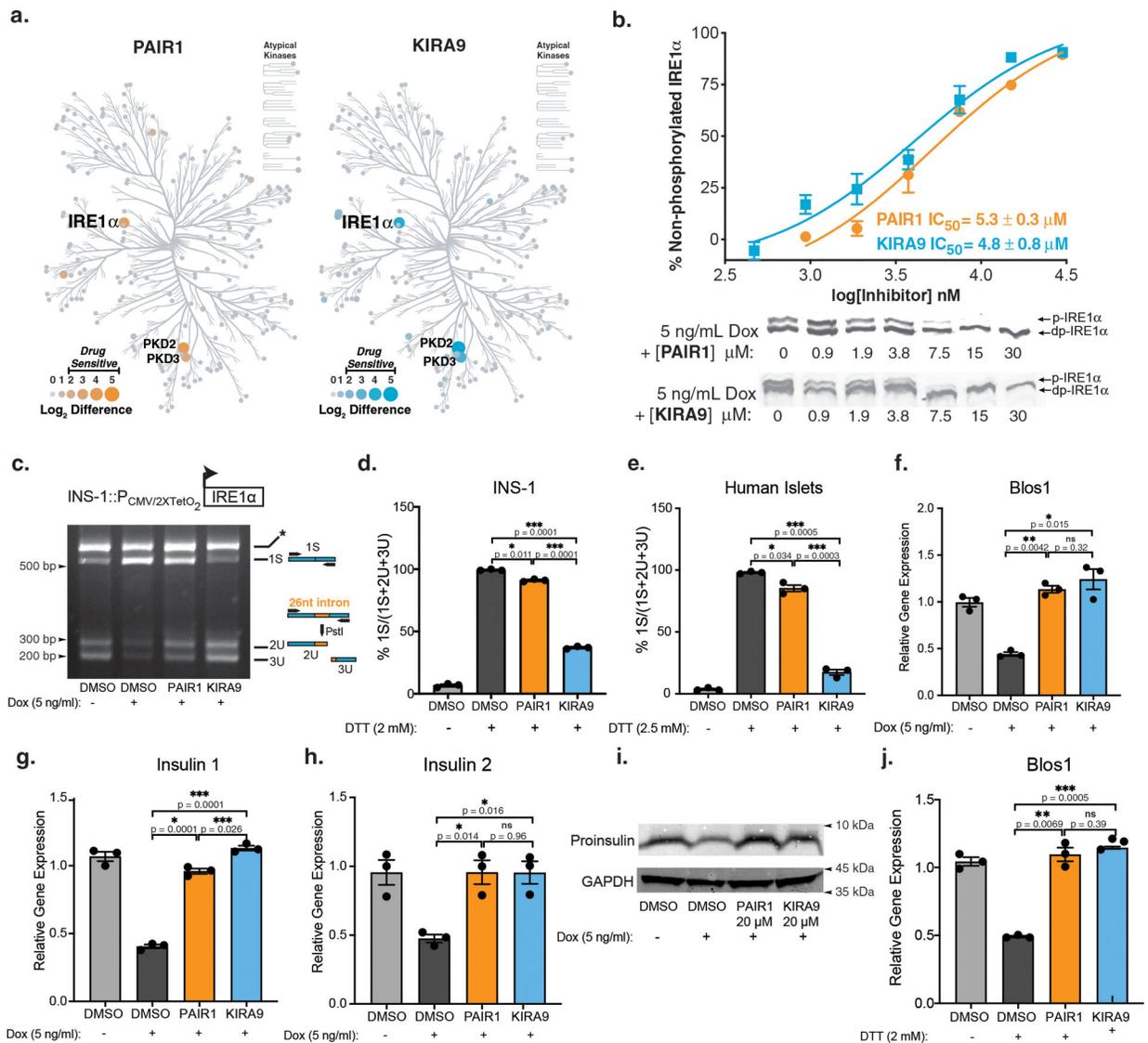
**Figure 4. PAIR1 spares XBP1 splicing but blocks RIDD outputs in cells**

(a) Kinome selectivity of PAIR1 and KIRA9 determined by kinobead profiling. Identified kinases are shown with gray circles. Circle size and color are scaled to the $\log_2$ ratio (difference in LFQ intensity) between DMSO and treatment with 10 μM of PAIR1 or KIRA9 (mean of n=4). Kinases reported as drug-sensitive ($\log_2$ Difference > 2) were required to show significance from a two-sample T-test with FDR = 0.05. (b) Immunoblots for total IRE1α from INS-1 cells expressing IRE1α under Dox control and treated with various concentrations of PAIR1 or KIRA9 followed by the addition of 5 ng/mL Dox (*bottom*). Samples were subjected to phostag SDS-PAGE and % non-phosphorylated IRE1α was determined from the ratio of non-phosphorylated IRE1α relative to total IRE1α (*top*). Values shown are the mean of n=3 biologically independent samples ± SEM. (c) EtBr-stained agarose gel of XBP1 cDNA amplicons from the cells described in (b) that were treated with DMSO, PAIR1, or KIRA9 followed by the addition of 5 ng/mL Dox. (d, e) Percent spliced XBP1 (quantified from PstI-digested XBP1 cDNA amplicons) from INS-1

cells (d) or human islets (e) treated with DMSO, PAIR1 (20 μM), or KIRA9 (20 μM) followed by the addition of 1,4-dithiothreitol (DTT). Data shown are the mean of n=3 biologically independent samples ± SEM. (f-h) qPCR of relative Blos1 (f), Insulin 1 (g), and Insulin 2 (h) mRNA levels from the cells described in (b) treated with DMSO, PAIR1 (20 μM), or KIRA9 (20 μM) followed by the addition of 5 ng/mL Dox. Data shown are the mean of n=3 biologically independent samples ± SEM. (i) Immunoblots for proinsulin from the cells described in (b) treated with DMSO, PAIR1 (20 μM), or KIRA9 (20 μM) followed by the addition of 5 ng/mL Dox. GAPDH shown as a loading control. (i) qPCR of relative Blos1 mRNA levels from INS-1 cells treated with DMSO, PAIR1 (20 μM), or KIRA9 (20 μM) followed by the addition of DTT. Data shown are the mean of n=3 biologically independent samples ± SEM. P values were calculated using two-tailed Student's t-test. $*P < 0.05$, $**P < 0.01$, $***P < 0.001$.
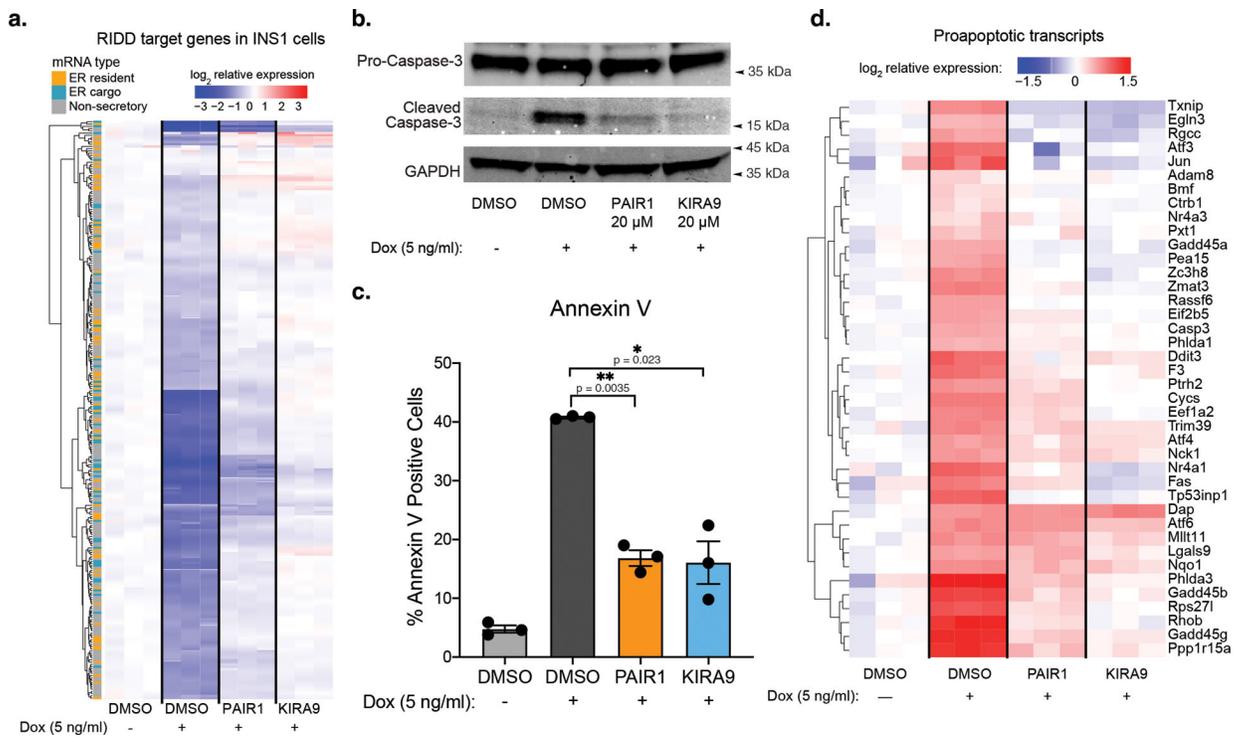
Figure 5. PAIR1 inhibits IRE1α-dependent mRNA decay and apoptosis

(a) Hierarchical analysis of gene expression changes from RNA-Seq profiling for INS-1 cells expressing IRE1α under Dox control and treated with DMSO, PAIR1 (20 μM) or KIRA9 (20 μM) followed by the addition of 5 ng/mL Dox. Data shown are the mean of n=3 biologically independent samples ± SEM. (b) Immunoblot of procaspase-3 and cleaved caspase-3 for cells subjected to the conditions described in Fig. 4i. The GAPDH blot from Fig. 4i is shown as a loading control. (c) Quantification of Annexin V staining for the cells described in Fig. 4b that were treated with DMSO, PAIR1 (20 μM), or KIRA9 (20 μM) followed by the addition of 5 ng/mL Dox. Data shown are the mean of n=3 biologically independent samples ± SEM. P values were calculated using two-tailed Student's t-test. *P < 0.05, **P < 0.01, ***P < 0.001 (d) Hierarchical analysis of pro-apoptotic genes expression changes from the RNA-Seq profiling described in (a).
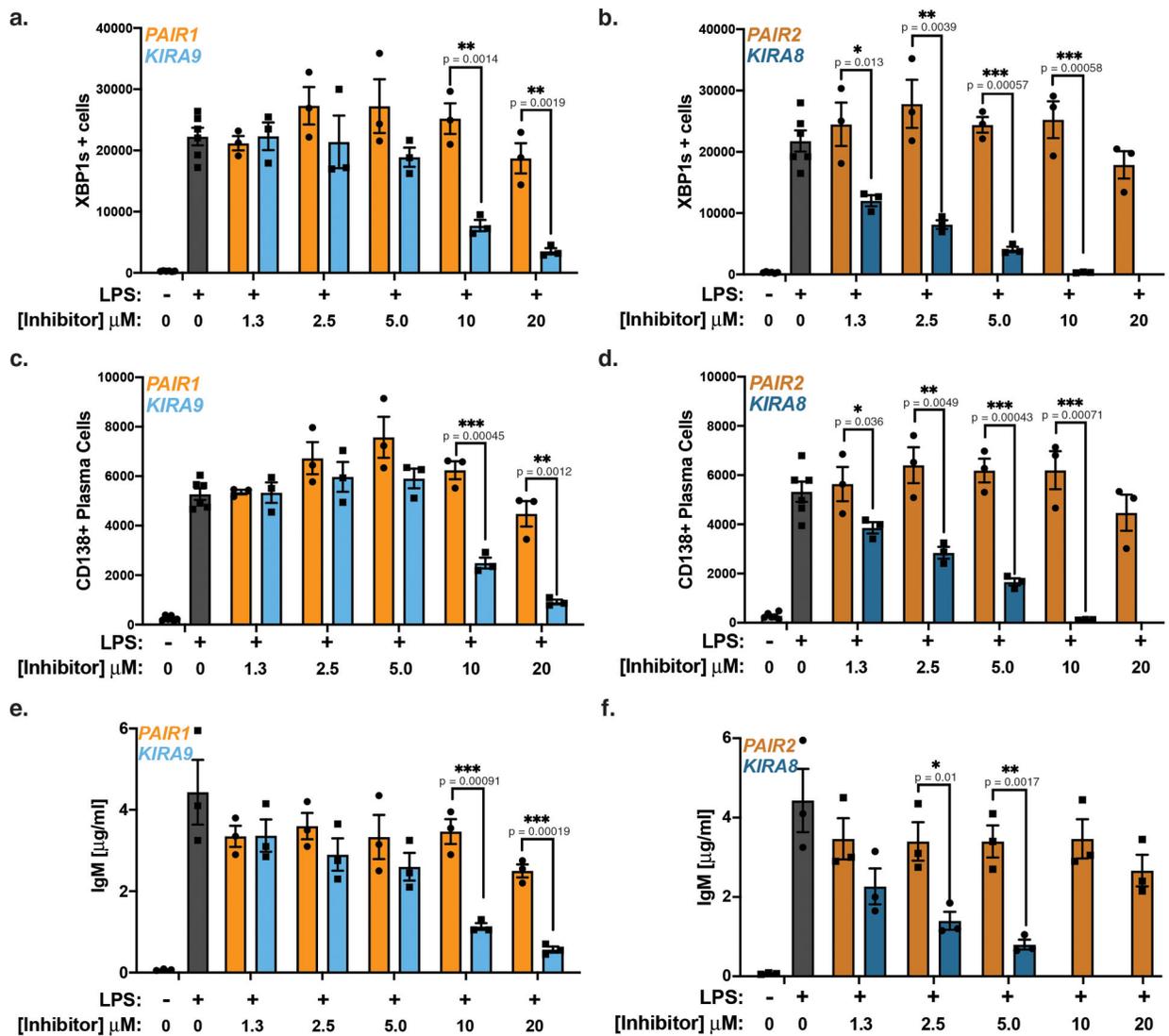
Figure 6. PAIRs and KIRAs differentially affect B-cell differentiation

Quantification of XBP1s+ B cells following treatment of mouse splenocytes with 1 μg/mL LPS for three days in the presence or absence of various concentrations of (a) PAIR1 (*orange*) or KIRA9 (*teal*) or (b) PAIR2 *(dark orange)* or KIRA8 *(dark blue)*. Quantification of CD138+ cells following treatment of mouse splenocytes with 1 μg/mL LPS for three days in the presence or absence of various concentrations of (c) PAIR1 (*orange*) or KIRA9 (*teal*) or (d) PAIR2 *(dark orange)* or KIRA8 *(dark blue)*. Gating scheme corresponding to (a-d) is shown in Extended Data Fig. 9. (e) ELISA quantification of IgM secretion for the splenocytes treated as described in (a, c). (f) ELISA quantification of IgM secretion for the splenocytes treated as described in (b, d). All data shown are the mean of n=3 biologically independent samples ± SEM. P values were calculated using one-tailed Student's t-test. *P < 0.033, **P < 0.002, ***P < 0.001. Data for 10 μM (f) and 20 μM (b,d,f) KIRA8 could not be generated due to cellular toxicity.